Projecting North American Climate over the Next 50 Years: Uncertainty due to Internal Variability*

CLARA DESER AND ADAM S. PHILLIPS

National Center for Atmospheric Research,+ Boulder, Colorado

MICHAEL A. ALEXANDER

NOAA/Earth System Research Laboratory, Boulder, Colorado

BRIAN V. SMOLIAK

University of Minnesota, Minneapolis, Minnesota

(Manuscript received 29 July 2013, in final form 30 October 2013)

ABSTRACT

This study highlights the relative importance of internally generated versus externally forced climate trends over the next 50 yr (2010–60) at local and regional scales over North America in two global coupled model ensembles. Both ensembles contain large numbers of integrations (17 and 40): each of which is subject to identical anthropogenic radiative forcing (e.g., greenhouse gas increase) but begins from a slightly different initial atmospheric state. Thus, the diversity of projected climate trends within each model ensemble is due solely to intrinsic, unpredictable variability of the climate system. Both model ensembles show that natural climate variability superimposed upon forced climate change will result in a range of possible future trends for surface air temperature and precipitation over the next 50 yr. Precipitation trends are particularly subject to uncertainty as a result of internal variability, with signal-to-noise ratios less than 2. Intrinsic atmospheric circulation variability is mainly responsible for the spread in future climate trends, imparting regional coherence to the internally driven air temperature and precipitation trends. The results underscore the importance of conducting a large number of climate change projections with a given model, as each realization will contain a different superposition of unforced and forced trends. Such initial-condition ensembles are also needed to determine the anthropogenic climate response at local and regional scales and provide a new perspective on how to usefully compare climate change projections across models.

1. Introduction

The combined effects of anthropogenic climate change and natural climate variability will determine Earth's climate trajectory in the coming decades. At the global scale, human-induced climate change is likely to dominate over internally generated variability for time periods longer than about a decade (e.g., Santer et al. 2011; Meehl et al. 2013). However, at regional and local scales, internal variability may be as important as anthropogenic climate change, even for intervals as long as the next 50 yr at middle and high latitudes (Deser et al. 2012a,b; Wallace et al. 2014). The partial masking of human-induced climate change by internal multidecadal variability is an important consideration for policy and planning efforts.

Internal climate variability arises from processes within and coupled interactions among the atmosphere, oceans, land, and cryosphere. While the ''memory'' of the atmosphere is generally limited to a few weeks, the atmospheric circulation exhibits long time-scale fluctuations characteristic of a random stochastic process (e.g., Lorenz 1963; Wunsch 1999; Feldstein 2000; Deser et al. 2012b). Indeed, extended atmospheric model control integrations exhibit decadal and longer-term fluctuations despite the

* Supplemental information related to this paper is available at the Journals Online website: http://dx.doi.org/10.1175/JCLI-D-13-00451.s1.

+ The National Center for Atmospheric Research is sponsored by the National Science Foundation.

Corresponding author address: Clara Deser, Climate and Global Dynamics Division, National Center for Atmospheric Research, Boulder, CO 80307.
E-mail: cdeser@ucar.edu

DOI: 10.1175/JCLI-D-13-00451.1

constant lower boundary conditions (Deser et al. 2012b). Such intrinsic atmospheric circulation variations induce regional changes in air temperature and precipitation on the multidecadal time scale (e.g., Deser et al. 2012b; Wallace et al. 2014, and references therein). Slow oceanic fluctuations may impart added persistence to the atmosphere. A prime example is the El Niño–Southern Oscillation (ENSO) phenomenon, a coupled ocean–atmosphere mode of interannual variability originating in the tropical Pacific that affects climate worldwide via atmospheric teleconnections (e.g., Horel and Wallace 1981). On longer time scales, fluctuations of the Atlantic thermohaline circulation and the Pacific and Atlantic Ocean gyre circulations contribute to low-frequency climate variability over the adjacent continents. In particular, the Atlantic multidecadal oscillation (AMO) has been implicated in long-term changes in Atlantic hurricane activity and precipitation over the Sahel, southeastern United States, and Brazil (e.g., Enfield et al. 2001; Zhang and Delworth 2006; Ting et al. 2009, 2011). Similarly, the Pacific decadal oscillation (PDO; Mantua et al. 1997) and interdecadal Pacific oscillation (IPO; Power et al. 1999) have contributed to low-frequency climate fluctuations over North America (Minobe 1997; Deser et al. 2004; Meehl et al. 2012) and Australia (Power et al. 1999). Despite their multidecadal character, the predictability of the AMO and PDO/IPO is limited to much shorter intervals ($<\sim$10 yr) because of their stochastic nature (Newman 2007; Msadek et al. 2010; Matei et al. 2012; Branstator et al. 2012; Newman 2013).

The climate response to rising concentrations of radiatively active chemical species including well-mixed greenhouse gases (GHGs) and tropospheric sulfate aerosols associated with human activities involves a complex set of feedbacks within the climate system: some of which are more certain than others (e.g., Solomon et al. 2007). In addition to anthropogenic factors, natural changes in radiative forcing of the climate system occur in association with variations in volcanic activity and solar output. Understanding such externally forced climate change, both human and natural in origin, remains a pressing challenge as evidenced by the considerable range of model sensitivities to the identical set of radiative forcings (Solomon et al. 2007).

Isolating the effects of anthropogenic climate change from those of internally generated variability requires ensembles of simulations with a given climate model, with each subject to the identical external forcing. This follows from the fact that any single model projection contains both intrinsic and externally forced contributions: it is only by averaging across ensemble members that the random sequences of internally generated variability in the individual realizations can be sufficiently muted to reveal the model's response to external forcing. [Note that this approach does not preclude the possibility that the forcing may affect the properties of the internal variability: for example, by changing its variance.] Once the externally forced response is obtained, it can be subtracted from each model run to find the contribution from internal variability. While it is common practice to average single runs from multiple models to obtain a robust estimate of anthropogenic climate change (e.g., the ''multimodel mean''; Solomon et al. 2007), this approach does not allow the isolation of internal variability in any given model simulation because structural differences between models can lead to different externally forced responses.

Using the phase 3 of the Coupled Model Intercomparison Project (CMIP3) multimodel archive, Hawkins and Sutton (2009, 2011) highlighted that structural differences among models constituted a greater source of uncertainty than internal variability in regional surface air temperature (precipitation) projections on time scales longer than 15 (30) yr. In their studies, internal variability was defined as the residual from a fourth-order polynomial fit to the time series over the next 100 yr in each run; that is, the externally forced response was equated with the fourth-order polynomial fit. With this definition, they effectively eliminated internal climate fluctuations with time scales longer than a few decades. Thus, they were unable to assess the full contribution of internal variability to uncertainty in regional climate projections over the next 50 yr.

The spread in projected climate trends over the next half century resulting from the superposition of internal variability and anthropogenic forcing has been examined with a 40-member ensemble of climate change simulations conducted with the National Center for Atmospheric Research (NCAR) Community Climate System Model, version 3 (CCSM3) (Deser et al. 2012a,b; Oshima et al. 2012; Kang et al. 2013; Hu and Deser 2013; Wettstein and Deser 2014; Wallace et al. 2014). These studies focused on various aspects of uncertainty due to internal variability, including signal-to-noise analysis; minimum ensemble size requirements; and time of emergence of the forced signals in near-surface air temperatures, precipitation, and atmospheric circulation patterns around the globe (Deser et al. 2012b; Oshima et al. 2012; Kang et al. 2013; Wallace et al. 2014). In addition, uncertainty in the magnitudes of future regional sea level rise and Arctic sea ice loss were assessed in Hu and Deser (2013) and Wettstein and Deser (2014), respectively. The impact of internal variability on 50-yr climate projections over North America was highlighted briefly in Deser et al. (2012a) and Wallace et al. (2014).

In this paper, we expand upon the early results of Deser et al. (2012a) and Wallace et al. (2014) to more

fully document the interplay between anthropogenic climate change and natural climate variability over North America during the next half century using two model ensembles, the 40-member CCSM3 discussed above and the 17-member ECHAM5/Max Planck Institute Ocean Model (MPI-OM; referred to as ECHAM5 for short). With such large sample sizes and two different models, we can more robustly determine the range of future climate outcomes. To the extent that natural variability over the next 50 yr is unpredictable, this range of future states represents the irreducible spread of the climate forecast. Knowledge of this spread will be important for the policy and decision-making communities.

We focus on two key climate parameters, near-surface air temperature and precipitation, in both winter (December–February) and summer (June–August). In addition to quantifying the relative amplitudes and spatial patterns of the externally forced and internally generated components of the climate projections in each model run, we investigate the contribution of the atmospheric circulation to the forced and free climate trends. Additionally, we apply a methodology for empirically removing from each realization the signature of atmospheric circulation-driven internal variability so that individual runs from different models can be directly compared.

The rest of the paper is organized as follows: Section 2 describes the models and experimental design, as well as the observational datasets used to evaluate aspects of the models' low-frequency variability. Section 3 provides results on the range of climate trends over the next 50 yr from each model ensemble, showing the relative contributions from internal variability and external forcing in terms of spatial maps, signal-to-noise ratios, and the likelihood that the trend will have a particular sign (e.g., warming, drying). It also demonstrates the role of the atmospheric circulation in the spread of climate trajectories and briefly compares decadal variability in the models with nature. Section 4 concludes with a summary of the main findings and a discussion of the results.

2. Models, experimental design, methods, and datasets

The primary model output used in this study is the 40-member ensemble of climate change simulations with the CCSM3 for the period 2000–60 described in Deser et al. (2012b), to which the reader is referred for complete details. CCSM3 is a comprehensive coupled atmosphere–ocean–sea ice–land general circulation model (for extensive documentation, see special issue of *Journal of Climate,* 2006, Vol. 19, No. 11) and a participant in CMIP3. The simulations are conducted at a horizontal resolution of approximately 2.8° latitude and 2.8° longitude (T42 spectral truncation). Each ensemble member undergoes the same external forcing: the main components of which are the Special Report on Emissions Scenarios (SRES) A1B greenhouse gas scenario (in which carbon dioxide concentrations increase from approximately 380 ppm in 2000 to approximately 570 ppm in 2060) and stratospheric ozone recovery by 2060, as well as smaller contributions from sulfate aerosol and black-carbon changes (see Meehl et al. 2006). Each ensemble member begins from identical initial conditions in the ocean, land, and sea ice model components (taken from the conditions on 1 January 2000 from a single twentieth-century CCSM3 integration) and slightly different initial conditions in the atmospheric model (taken from different days during December 1999 and January 2000 from the same twentieth-century CCSM3 run). Thus, the spread amongst the different members represents the irreducible uncertainty of the forecast (e.g., arising from unpredictable internally generated variability). The sensitivity of the climate system to small perturbations in initial conditions is characteristic of a nonlinear deterministic system as elucidated by Lorenz (1963). Perturbing the initial state of the ocean in addition to the atmosphere may add to the uncertainty of the climate forecast, but we have not explored this aspect here.

We also make use of the 17-member ensemble of climate change simulations with ECHAM5, which is also a CMIP3 model (for details, see Roeckner et al. 2003; Sterl et al. 2008). The ECHAM5 runs are conducted at a horizontal resolution of approximately 1.875° in latitude and longitude (T63 spectral truncation). The experimental design for the ECHAM5 ensemble is very similar to that for CCSM3. In particular, the ECHAM runs are subject to the same external forcing as CCSM3, except for stratospheric ozone, which was kept constant. This difference is expected to have minimal impact on the comparison between the two models, given that our focus is on North America and the largest ozone changes occur over the South Pole. Each ensemble member begins from identical initial conditions in the ocean, land, and sea ice model components (taken from the conditions on 1 January 1950 from a single twentieth-century integration) and slightly different initial conditions in the atmospheric model obtained by perturbing the initial state of the atmosphere using Gaussian noise with an amplitude of 0.1°C (Roeckner et al. 2003). The ECHAM ensemble covers the period 1950–2100.

We analyze the period 2010–60 from each model ensemble and compute linear trends over this 51-yr period for winter (December–February) and summer (June–August) separately. The trend values are reported in

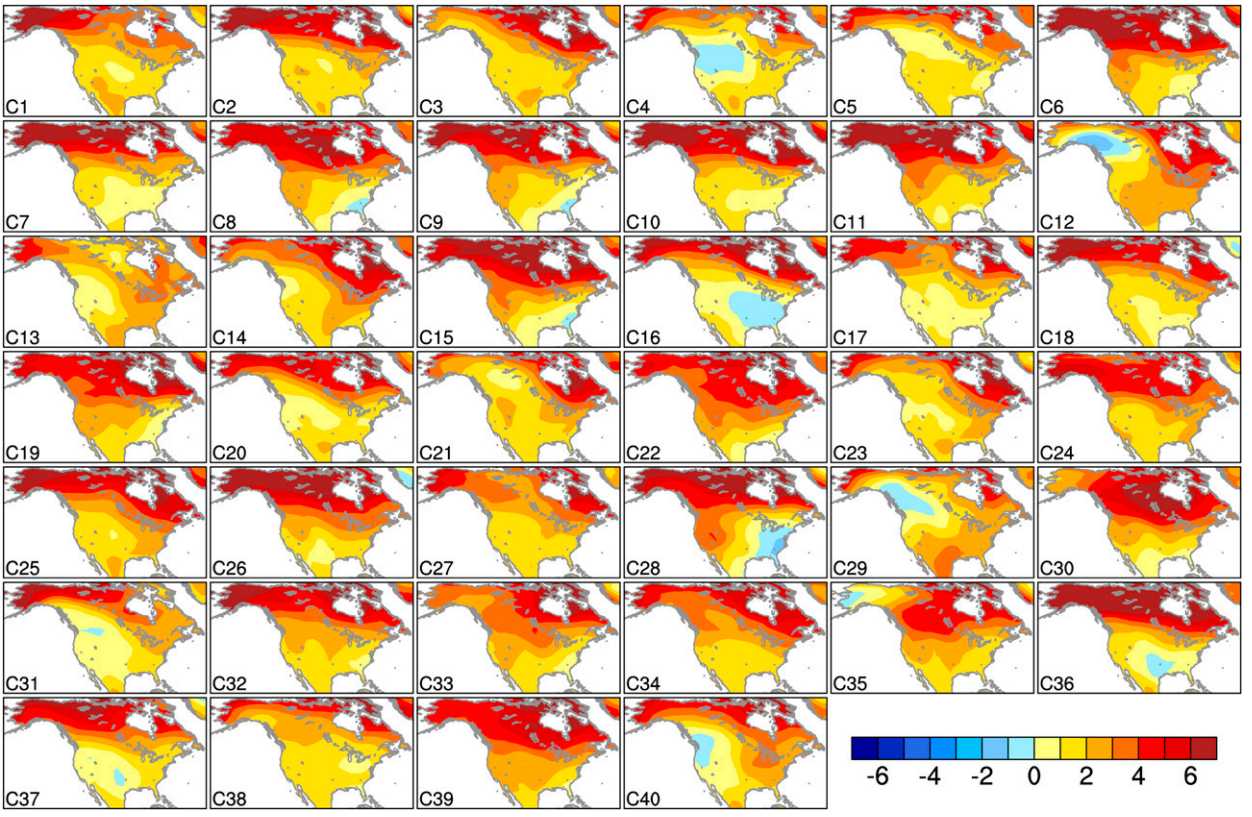

FIG. 1. Winter SAT trends [2010–60; °C (51 yr)$^{-1}$] from each of the 40 CCSM3 ensemble members.

physical units (e.g., as the total linear change over the 51-yr period; e.g., in °C for air temperature and mm day^{-1} for precipitation). Similar results are obtained using epoch differences between 2051–60 and 2010–19 in place of linear trends (see also Deser et al. 2012b).

We make use of the following observational datasets to validate the models' decadal variability: air temperature from the Merged Land–Ocean Surface Temperature analysis (MLOST) version 3.5 (Vose et al. 2012) on a 5° latitude/longitude grid; precipitation from the Global Precipitation Climatology Centre (GPCC; Becher et al. 2013) dataset on a 1° grid; and sea level pressure from the Twentieth-Century Reanalysis (20CR; Compo et al. 2011) on a 2° grid. We use data over the period 1900–2010 for each dataset.

3. Results

a. Overview of SAT and precipitation trends

The complete set of seasonal surface air temperature (SAT) and precipitation trends projected for 2010–60 from each run of CCSM3 and ECHAM5 is presented in Figs. S1–S6 in the supplementary materials. Here we show a subset of the results to illustrate some key points. Winter SAT trends over the next 50 yr display considerable diversity across the CCSM3 40-member ensemble, despite each simulation being subject to identical radiative forcing (Fig. 1). For example, some ensemble members exhibit amplified warming (>5°C) over Canada (runs 6, 15, 26, and 36) while others show cooling over portions of the United States (runs 4, 16, 28, 36, and 40). The canonical signature of poleward amplification is evident in many of the runs, while others lack this structure, favoring instead an east–west contrast in warming magnitude (runs 12, 13, 29, 33, and 35). The 17-member ECHAM5 ensemble exhibits qualitatively similar diversity in winter SAT trends (Fig. S3).

Figure 2 shows the projected (2010–60) trends in summer precipitation for each of the 40 CCSM3 ensemble members. The largest amplitude trends (± 1 mm day^{-1}) generally occur over the central United States: however, their polarity varies considerably from member to member. For example, runs 3, 11, 12, 26, and 27 exhibit positive precipitation trends in this region while runs 1, 9, 16, 21, and 39 show negative trends. A similar diversity in the polarity of summer precipitation trends is present in the 17-member ECHAM5 ensemble (Fig. S6). In fact, summer precipitation trends in ECHAM5 show somewhat

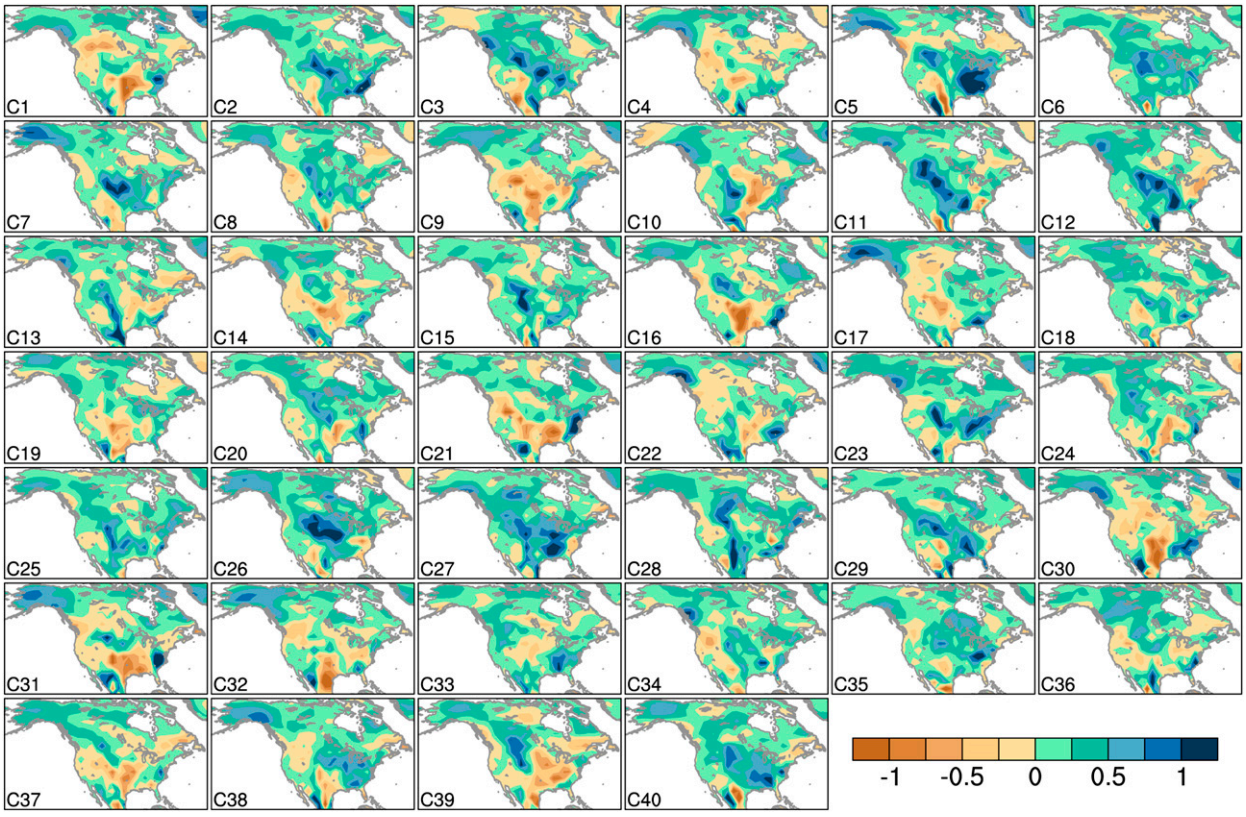

FIG. 2. Summer precipitation trends [2010–60; mm day^{-1} (51 yr)$^{-1}$] from each of the 40 CCSM3 ensemble members.

larger amplitudes and member-to-member variation compared to CCSM3. Recall that each individual model realization represents a plausible outcome (subject to model limitations) for future precipitation trends over North America and that the differences within a single model ensemble are due solely to internally generated climate variability.

b. *Partitioning of total trends into internal and forced components*

The variety of projected climate trends in individual model realizations results from the superposition of internal climate variability and the response to external forcing (i.e., GHG increases). To illustrate this point, we partition the total trends into contributions from the forced response (obtained by averaging all ensemble members) and the internal variability (obtained by subtracting the forced response from the total trend). Examples of this decomposition are given in Figs. 3 and 4 based on CCSM3; similar results are obtained from ECHAM5 (not shown). Figure 3a shows winter SAT trends for members 16 and 22, the runs with the least and most warming over the contiguous United States, respectively. The total trends (Fig. 3a, left) are markedly different, with run 16 showing little warming over most of the contiguous United States (<1°C in the west and slight cooling in the east) coupled with high amplitude (>6°C) warming near the Arctic border; whereas run 22 shows a more diffuse pattern of warming that extends southward over much of the continent. The forced component of these trends exhibits the expected signature of poleward amplification, with regions adjacent to the Arctic Ocean warming by 5°–6°C compared to 1°–2°C over most of the contiguous United States (Fig. 3, right). The internally generated or natural component of the trends exhibit continental-scale patterns with maximum amplitudes of approximately 1°–3°C (e.g., comparable to the forced response over the contiguous United States; Fig. 3a, center). Specifically, internal variability contributes to widespread cooling over the United States and southern Canada, as well as warming over northern Canada and Alaska, in run 16, whereas it contributes to warming over the middle of the continent and slight cooling to the north and south in run 22. Averaged over the contiguous United States, the SAT trend in run 16 (0.8°C) results from a balance between the response to radiative forcing (2.1°C) and internal variability (−1.3°C). For run 22, the U.S.-average

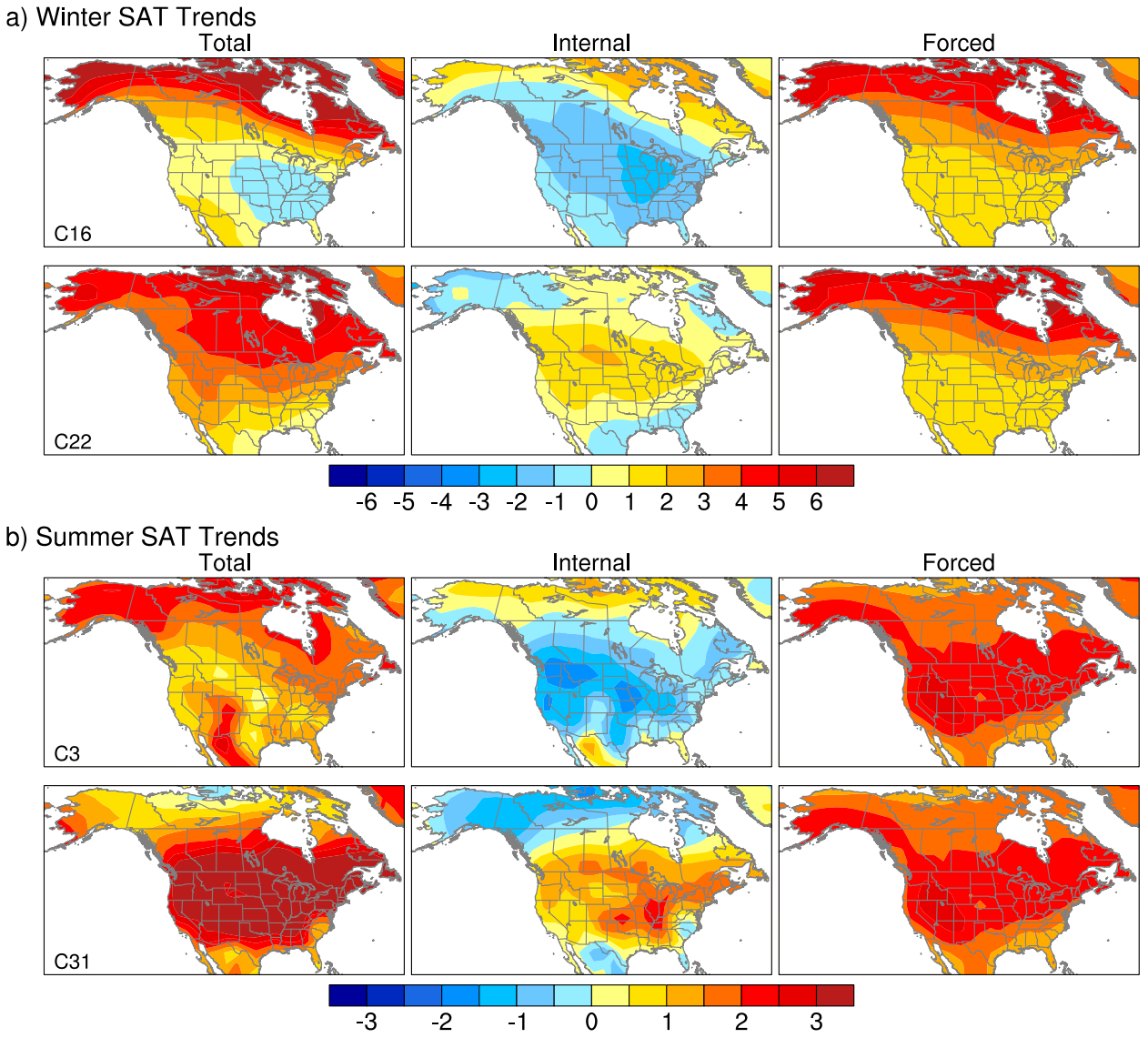

FIG. 3. (left) Total 2010–60 SAT trends decomposed into (center) internal and (right) forced components for two contrasting CCSM3 ensemble members. Results shown for (a) winter, runs 16 and 22, and (b) summer, runs 3 and 31. Color bar units are degrees Celsius per 51 yr.

SAT trend (3.4°C) is composed of the forced response (2.1°C) augmented by internal variability (1.3°C).

Summer SAT trends also exhibit considerable range in magnitude and spatial pattern across the CCSM3 ensemble (Fig. 3b; see also Fig. S1). For example, run 3 shows muted warming (<1.5°C) over much of the contiguous United States accompanied by larger warming (1.5–3.5°C) over northern Canada and Alaska, while run 31 shows strong SAT increases (>3°C) over the United States accompanied by weaker warming to the north (<1°C; Fig. 3b). The contribution of internal variability to the summer SAT trends in the two runs shows similar large-scale patterns to those in winter, with out-of-phase behavior between northern Canada/Alaska and the contiguous United States. In terms of magnitude, the unforced contribution is generally less than the forced contribution, except over parts of the U.S. Midwest, where they are comparable. Averaged over the contiguous United States, the SAT trend in run 3 (1.1°C) results from radiative forcing (2.1°C) partially offset by internal variability (−1.0°C). For run 31, the U.S.-average SAT trend (3.3°C) is composed of the forced response (2.1°C) augmented by internal variability (1.2°C).

The diversity of precipitation trends across the CCSM3 ensemble indicates a large role for internal variability compared to radiative forcing in both seasons (Fig. 4; see

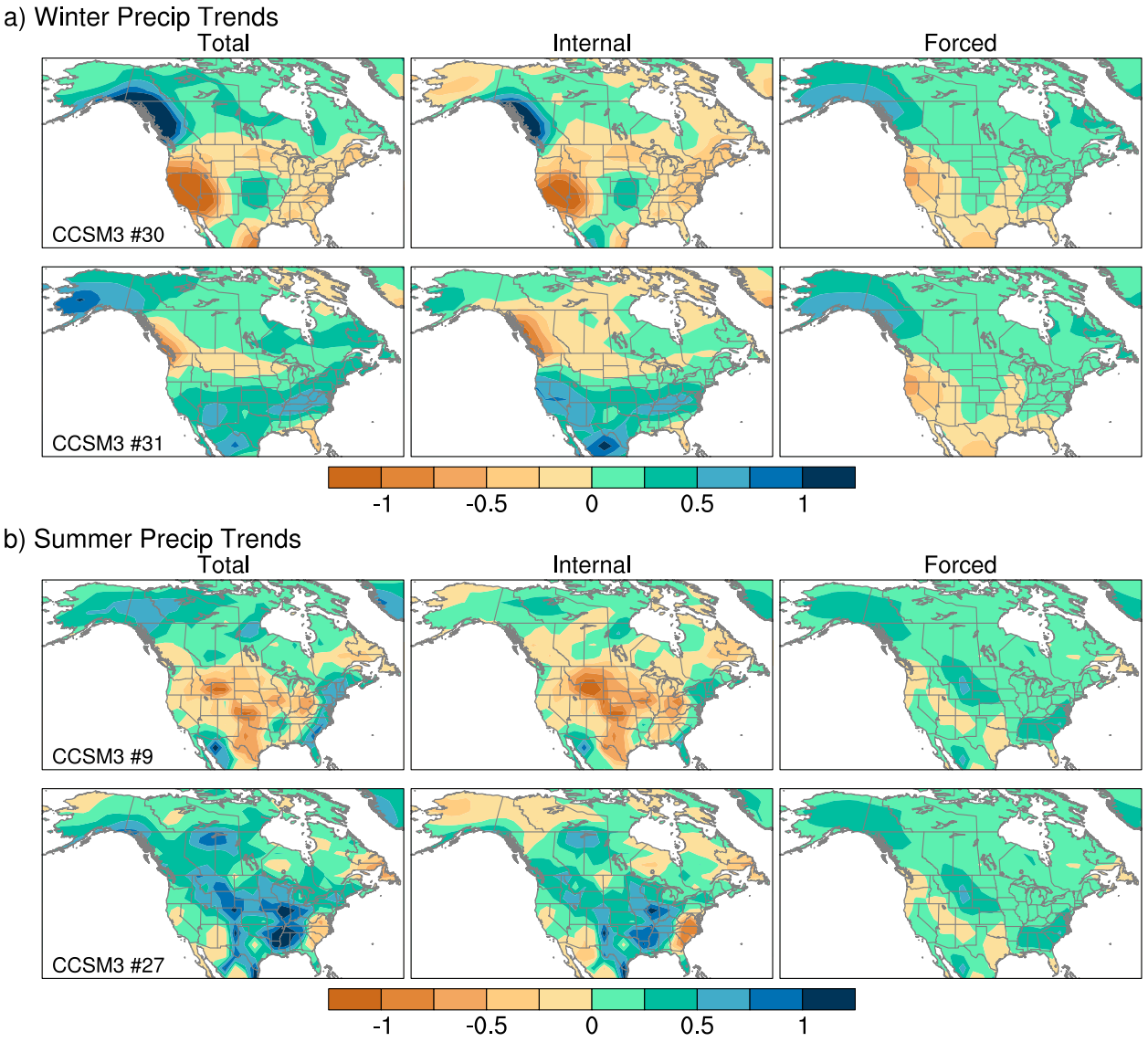

FIG. 4. As in Fig. 3, but for precipitation. Results shown for (a) winter, runs 30 and 31, and (b) summer, runs 9 and 17. Color bar units are millimeters per day per 51 yr.

also Figs. 2 and S2). For example, in winter, the total precipitation trend in run 30 shows a dipole pattern along the west coast of North America, with large increases ($>1\,\text{mm day}^{-1}$) over Canada and similar amplitude decreases over the United States (Fig. 4a). A contrasting pattern is found for run 31, which shows widespread precipitation increases ($\sim 0.5\,\text{mm day}^{-1}$) across the southern United States, accompanied by drying (moistening) along the west coast of Canada (Alaska) in the total field (Fig. 4a). It is clear that internal variability dominates over radiative forcing in the areas of maximum trend amplitude and that radiative forcing is responsible for the modest moistening (0.2–$0.3\,\text{mm day}^{-1}$) across Canada common to both runs (Fig. 4a).

In summer, CCSM3 ensemble member 9 shows drying over the interior United States in the total field, where all of which derives from internal variability, while ensemble member 27 shows broadscale moistening over the same region, where nearly all of which is due to internal variability (Fig. 4b). Averaged over the contiguous United States, the total summer precipitation trend in run 9 ($-0.18\,\text{mm day}^{-1}$) results from internal variability ($-0.31\,\text{mm day}^{-1}$) partially offset by the forced response ($0.13\,\text{mm day}^{-1}$), while that in run 27 ($-0.44\,\text{mm day}^{-1}$) derives from mainly internal variability ($0.31\,\text{mm day}^{-1}$) plus the forced response.

Two important points emerge from Figs. 3 and 4. First, the unforced component of SAT and precipitation

trends over the interval 2010–60 exhibit large-scale spatial coherence as opposed to small-scale noise. Second, the magnitude of the unforced component of the 2010–60 trend can be as large as (in the case of SAT, especially in winter) or larger than (in the case of precipitation) that of the forced component. Similar points obtain for ECHAM5 (not shown). Taken together, these results have important implications for resource management and adaptation. For example, water resource managers must plan for a range of future conditions that span broad geographical regions.

The diversity of SAT and precipitation trends within the CCSM3 and ECHAM5 ensembles indicates that not only is a large set of simulations needed to define the forced climate response in a single model but also the interpretation of any single model realization as the forced climate response is problematic, especially on local and regional scales over North America. Additionally, both models give the qualitative impression that future precipitation trends exhibit higher uncertainty than future SAT trends, an aspect that will be quantified in the next section.

c. *Quantifying the relative contributions of internal variability and external forcing*

The results shown above give a qualitative impression of the range of patterns and amplitudes of projected SAT and precipitation trends over the next 50 yr because of external radiative (i.e., GHG) forcing and internal variability. Here we provide a quantitative assessment using a simple signal-to-noise analysis. Figure 5a compares the forced SAT trends in the two models, estimated by averaging over all ensemble members, and Fig. 5b shows the standard deviation of the SAT trends (e.g., internal variability) across the ensemble members in each model. The signal-to-noise ratio (SNR) between the forced SAT trend and the internal variability of the SAT trends is shown in Fig. 6 (top). These standard metrics convey useful information about the magnitudes of the forced and internally generated components of future climate change, although they do not convey anything about the spatial coherence of the internal contribution (recall Figs. 3 and 4).

The forced SAT responses in the two models are generally comparable in terms of pattern and amplitude, with poleward-intensified warming in winter and relatively homogenous and weak warming in summer (Fig. 5, top). The more mottled appearance of the warming in ECHAM5 compared to CCSM3 may be partly due to its smaller ensemble size and higher spatial resolution. The internal variability of the SAT responses is stronger in winter than summer in both models, especially over Canada and Alaska (Fig. 5, bottom). However, CCSM3 shows larger internal variability of SAT trends compared to ECHAM5 at many locations in both seasons. Consequently, SNRs are somewhat higher for ECHAM5 compared to CCSM3 (Fig. 6, top). However, the SNR spatial distributions are similar between the models, with relatively low values over the midsection of the continent in winter (1–2 in CCSM3 compared to 3–4 in ECHAM5), and high values (4–5) over the western and eastern United States in summer (and extending to southern Canada in ECHAM5). Over the United States, the SNR is generally higher in summer than winter in both models. It is worth noting that the spatial pattern of the SNR is mainly determined by the pattern of the internal variability in summer and by a combination of the patterns of the forced response and the internal variability in winter.

The forced precipitation trends at high latitudes are broadly similar between the two models, with the largest increases along the Gulf of Alaska coast in winter and more moderate but widespread increases over Canada and Alaska in both seasons (Fig. 7, top). The forced trends over the contiguous United States show less agreement between the two models, especially in summer, with many regions lacking a statistically significant response. In particular, ECHAM5 shows statistically significant summer drying over Mexico and parts of Texas, New Mexico, and Arizona, whereas CCSM3 exhibits wetter conditions of marginal statistical significance in these areas. In addition, the eastern United States shows significant precipitation increases in both seasons in ECHAM5 but only in summer in CCSM3. The spatial patterns of internal precipitation trend variability are similar for the two models, with the largest values along the entire Pacific coast and in southeastern United States in winter and in the central and eastern United States and southern Alaska in summer (Fig. 7, bottom). Over the United States, variability is generally higher in ECHAM5 than CCSM3 in winter and vice versa in summer (comparison to observations is given in section 3g). An important result is that SNR is considerably lower for precipitation trends than SAT trends, with values generally <1 over the contiguous United States and values mostly <2 over Canada and Alaska in both models and seasons (Fig. 6, bottom).

d. *Chance of positive trends*

From these large ensembles, one can quantify the chances that temperature or precipitation will increase (or decrease) over the coming decades by counting the number of runs with a positive trend divided by the total number of runs for each model. We reiterate that in these model ensembles, the reason why individual runs may show opposite-signed trends at a given location is due to unpredictable, internally generated variability. Figure 8 shows the results for winter SAT and precipitation trends

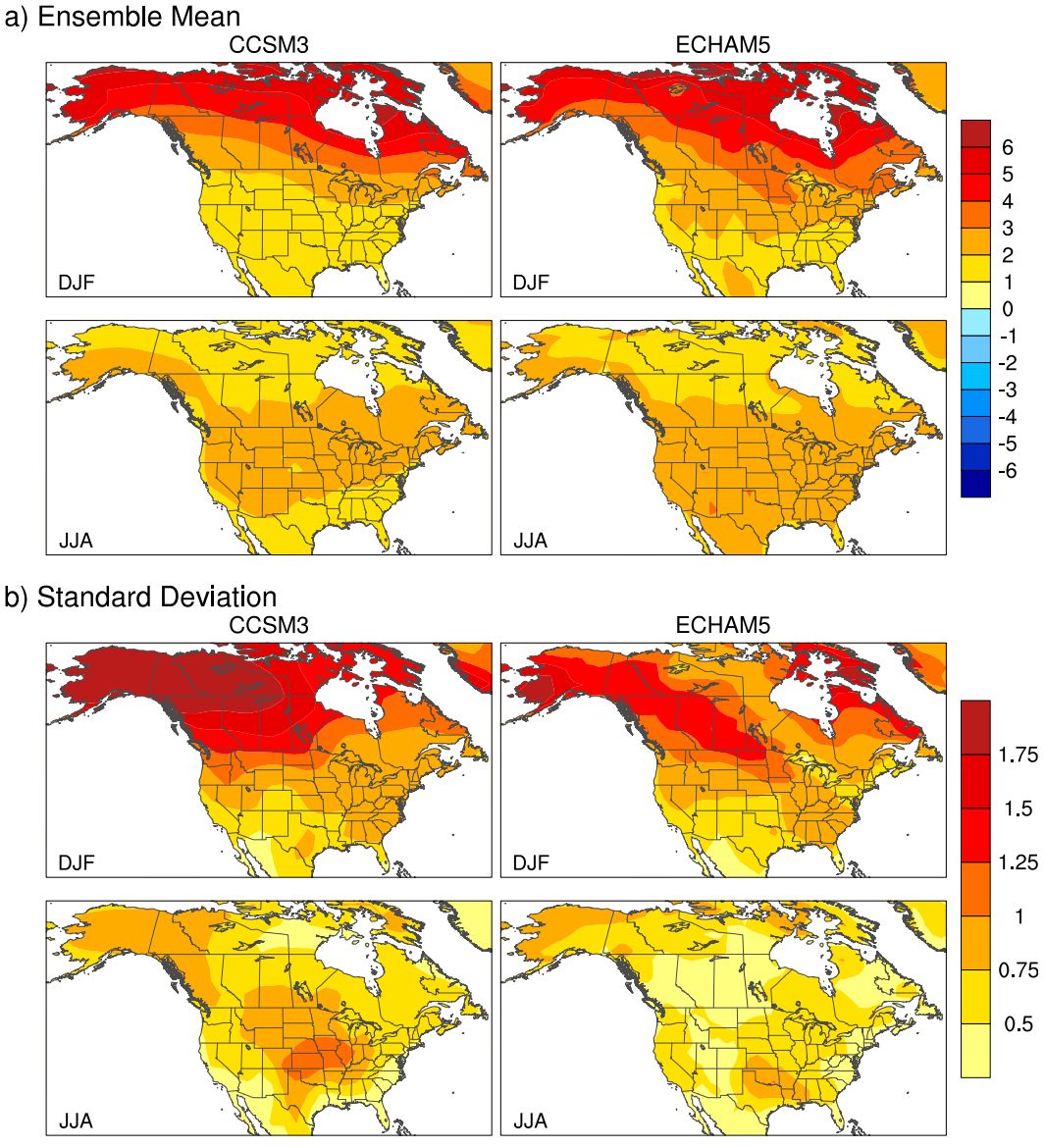

FIG. 5. SAT trends 2010–60 [°C (51 yr)$^{-1}$]: (a) ensemble-mean and (b) standard deviation from (left) CCSM3 and (right) ECHAM5. In (a),(b): for (top) December–February (DJF) and (bottom) June–August (JJA). All values in (a) are significant at the 95% confidence level.

over the next 50 yr (2010–60) in winter (top panels) and summer (bottom panels) for both CCSM3 and ECHAM5. Over the next 50 yr, both models show a better than 95% chance that winters will warm at all but a few locations; winter precipitation trends, on the other hand, are less certain over much of the contiguous United States, with the most robust precipitation trends occurring over northern Canada where chances of moistening generally exceed 85% and to a lesser extent over the western United States, where chances of drying exceed approximately 65% (note that a low chance of a positive precipitation trend implies a high chance of a negative precipitation trend). Broad areas of the eastern United States in winter and much of the continent in summer exhibit approximately equal odds (35%–65%) of drying and moistening trends over the next 50 yr; a notable exception is over the desert southwest in summer where chances of a drying trend are >75% in ECHAM5.

The sign of the trends is less certain over the next 25 yr (2010–35) compared to the next 50 yr (Fig. 9). Chances of warming over the next 25 yr are 55%–75% over the northwestern and southeastern portions of the continent in winter, depending on the model. Even in summer over the next 25 yr, there are regions where the chance of

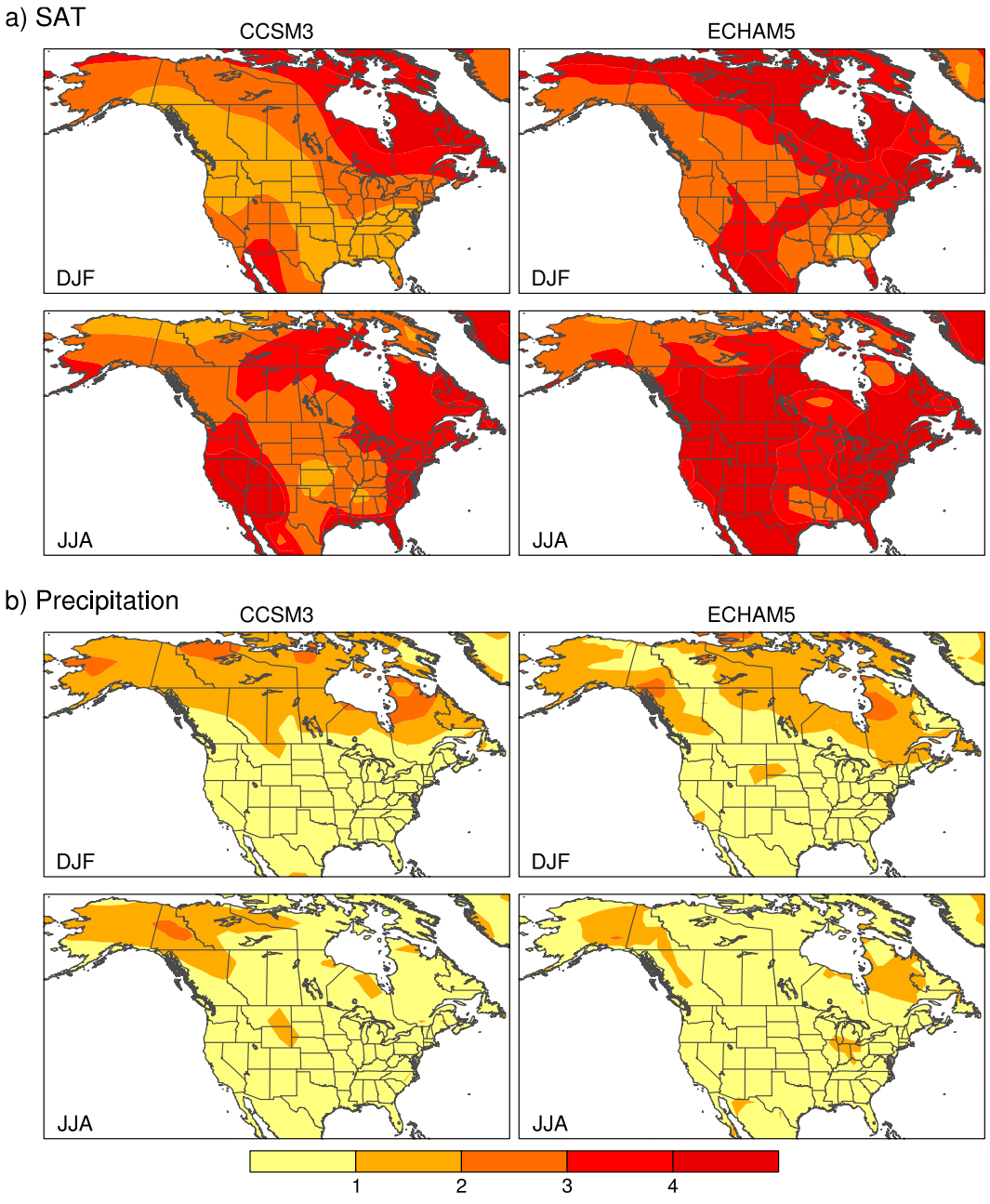

FIG. 6. Signal-to-noise ratio maps for (a) SAT and (b) precipitation trends during 2010–60 from (left) CCSM3 and (right) ECHAM5 in DJF and JJA. Signal to noise is defined as the absolute value of the forced (ensemble mean) trend divided by the standard deviation of trends across the individual ensemble members.

warming is reduced to 65%–75%, although the two models disagree on their location. The models show consistent results for the western United States, which has a better than 95% chance of warming over the next 25 yr. Unlike SAT, the sign of precipitation trends over the next 25 yr is highly uncertain in both model ensembles, with most areas falling in the 35%–75% range. These results have implications for the detection of future forced climate change at any given location, as well as planning and mitigation efforts.

e. Internal variability of future climate trends: Role of the atmospheric circulation

What are the physical mechanisms underlying internal variability of projected climate trends in the next 50 yr over North America? It is useful to consider two broad

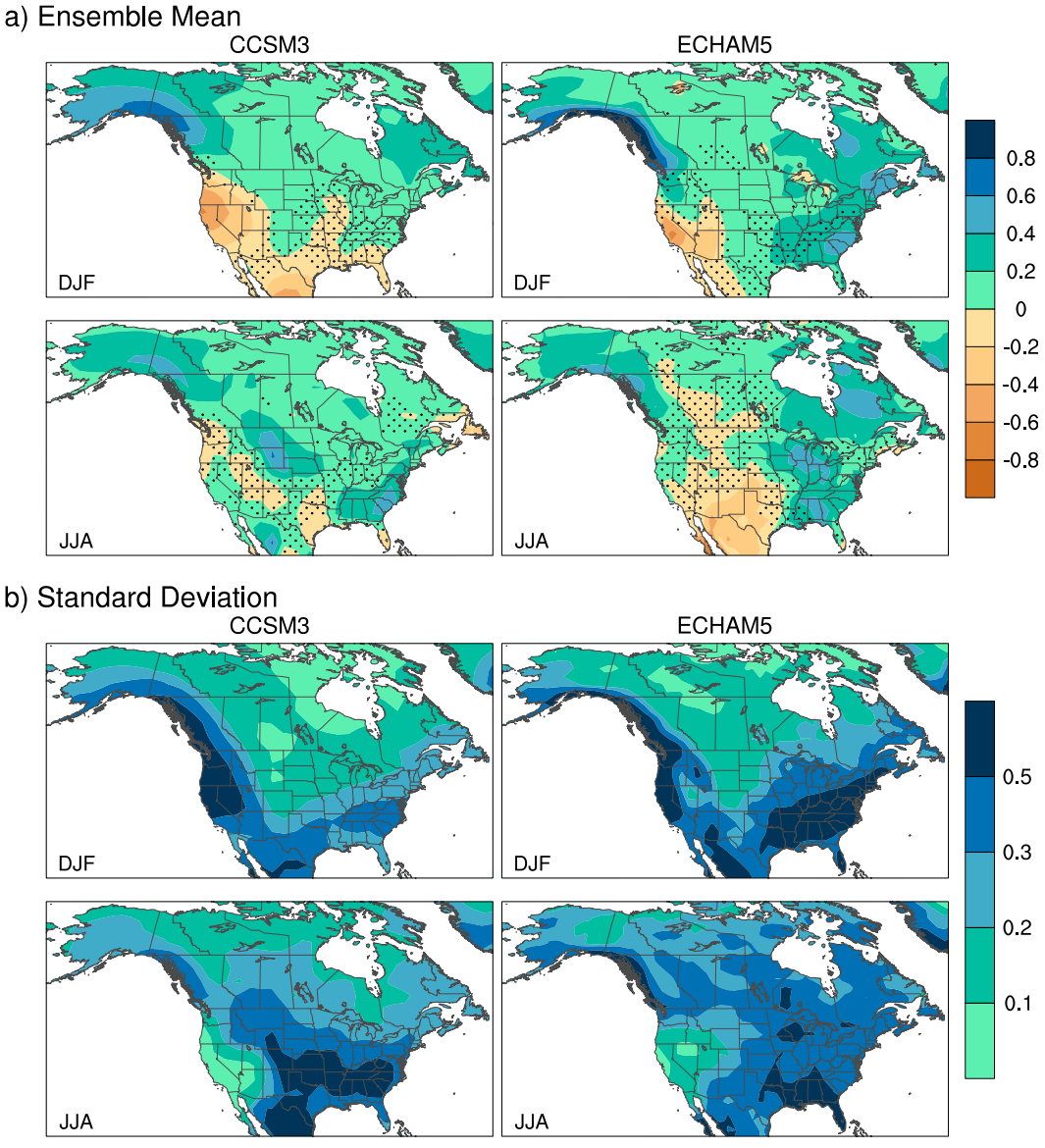

FIG. 7. As in Fig. 6, but for precipitation trends for 2010–60 [mm day^{-1} (51 yr)$^{-1}$]. (a) Stippling indicates values not significant at the 95% confidence level.

classes of mechanisms: thermodynamic and dynamical. Thermodynamic processes include effects of internal variability in clouds, water vapor, snow cover, soil moisture, sea surface temperatures, and sea ice conditions upon the heat and moisture budget of the overlying atmosphere, in the absence of atmospheric circulation changes. Dynamical mechanisms relate to internal variations in the atmospheric circulation, which alter SAT and precipitation via changes in airmass trajectories and their associated advection of heat and moisture. Numerous studies have demonstrated the importance of fluctuations in the large-scale atmospheric flow, which have been shown to account for a large fraction of the variability in SAT and precipitation over North America on time scales ranging from weeks to decades (e.g., Wallace et al. 1995; Hurrell 1996; Thompson et al. 2009; Wallace et al. 2012). Although it is conceptually useful to consider the two classes of mechanisms independently, significant feedbacks may exist between them. For example, circulation-induced changes in precipitation may alter snow cover, soil moisture, and cloudiness; these in turn may affect SAT by altering the surface radiation balance. Such feedbacks may be particularly strong in summer (e.g., Fischer et al. 2007; Hoerling et al. 2014), evidenced in part by the inverse correlation between interannual variations in SAT and precipitation

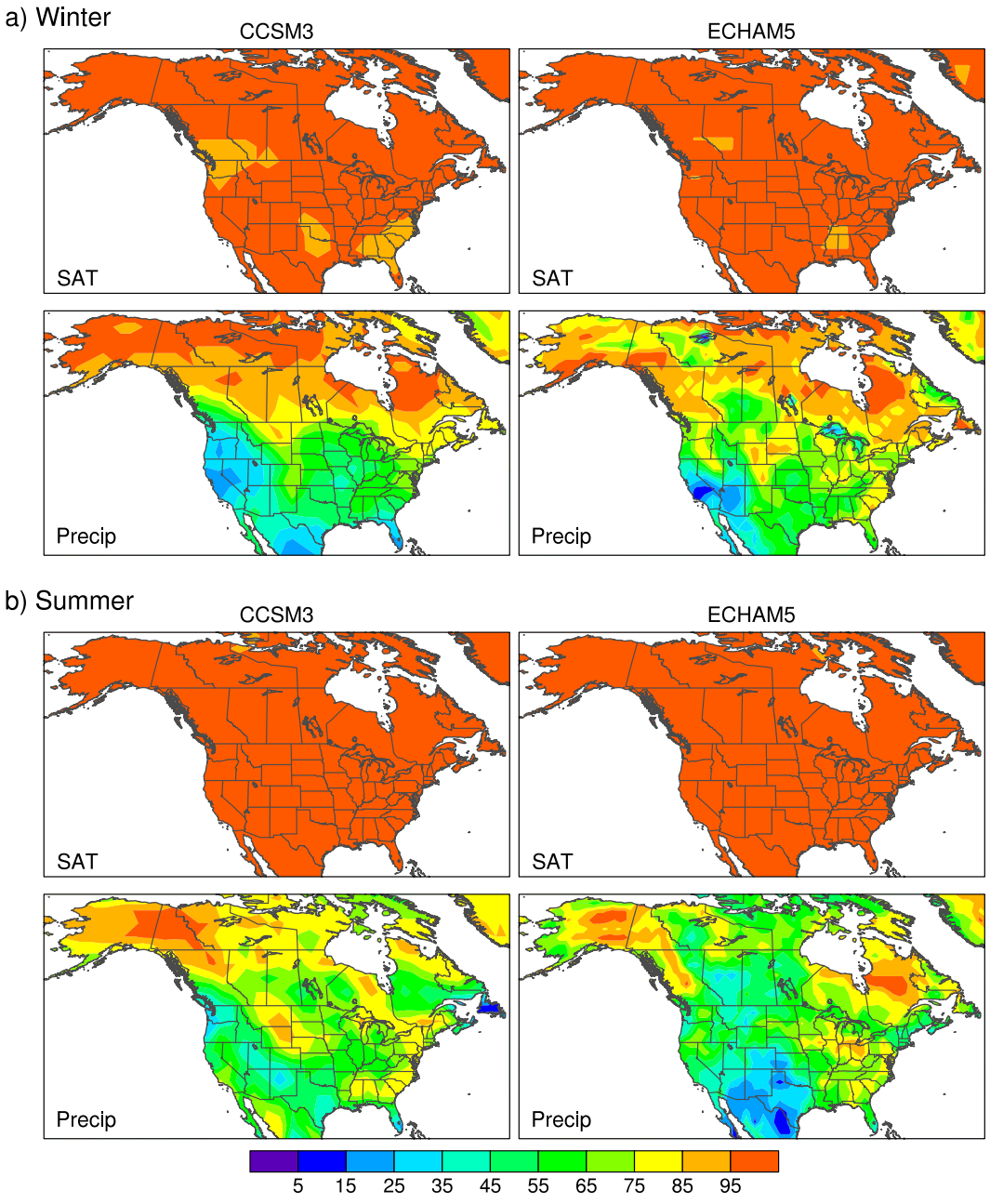

FIG. 8. Chance (%) of a positive trend in SAT and precipitation over the period 2010–60 during (a) winter and (b) summer from the (left) CCSM3 and (right) ECHAM5 ensembles. Note that a low chance implies a high chance of a negative trend.

over much of the United States (e.g., Trenberth and Shea 2005).

We hypothesize that the spread in climate change projections within a given model ensemble is largely due to dynamically induced internal variability, particularly during winter. As a first step in evaluating the role of the atmospheric circulation, we show winter sea level pressure (SLP) trends in two contrasting runs from the CCSM3 ensemble, along with accompanying trends in SAT and precipitation. As before, the total trends are decomposed into contributions from internal variability and the forced response. Run 29 features positive SLP trends over the North Pacific, with maximum amplitude of approximately 6 hPa, compared to negative SLP trends of similar magnitude in run 6 (Fig. 10, left). The opposite-signed circulation trends are associated with

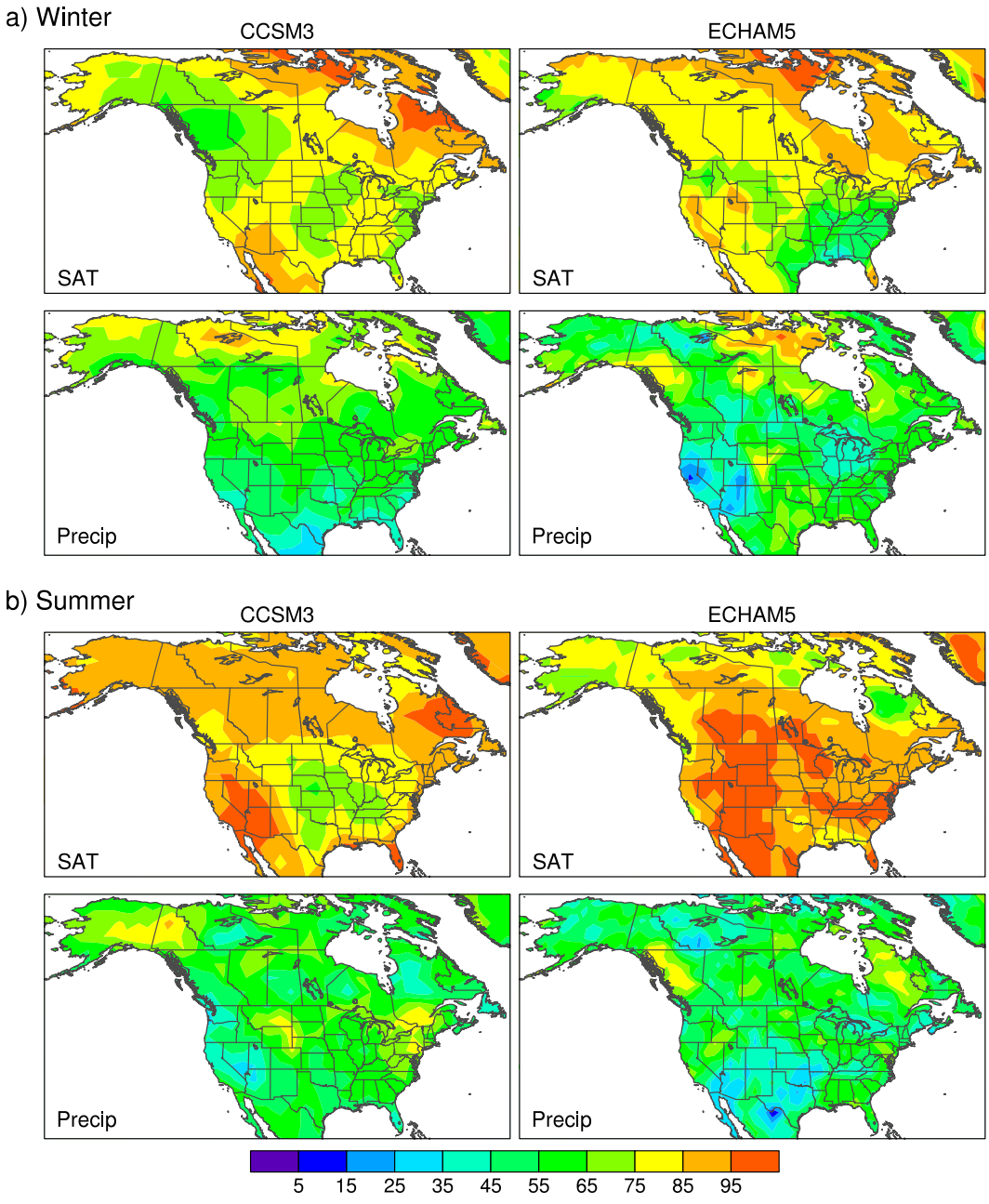

FIG. 9. As in Fig. 8, but for 2010–35.

different airmass trajectories, with run 29 bringing cold air from the north down into Canada and run 6 bringing warm maritime air up from the south into western Canada. The imprint of these different trends in airflow can be seen in the total SAT trend field. The effect of the circulation on SAT is more readily discernible in the unforced component of the trends (Fig. 10a, center). The internal component of the two SLP trend patterns is nearly equal and opposite, with positive values over the North Pacific and negative values over eastern Canada in run 29 and reversed polarity in run 6. These SLP trend patterns give rise to northerly (southerly) wind trends over Canada in run 29 (6), qualitatively explaining the cooling (warming) trends (Fig. 10a, center).

The relationship between the SLP and SAT trends is very different for the forced component compared to the unforced component (Fig. 10a, right). The forced SAT trends are dominated by a northward-intensified warming pattern, with little discernible influence from the forced SLP trend distribution. It is also noteworthy

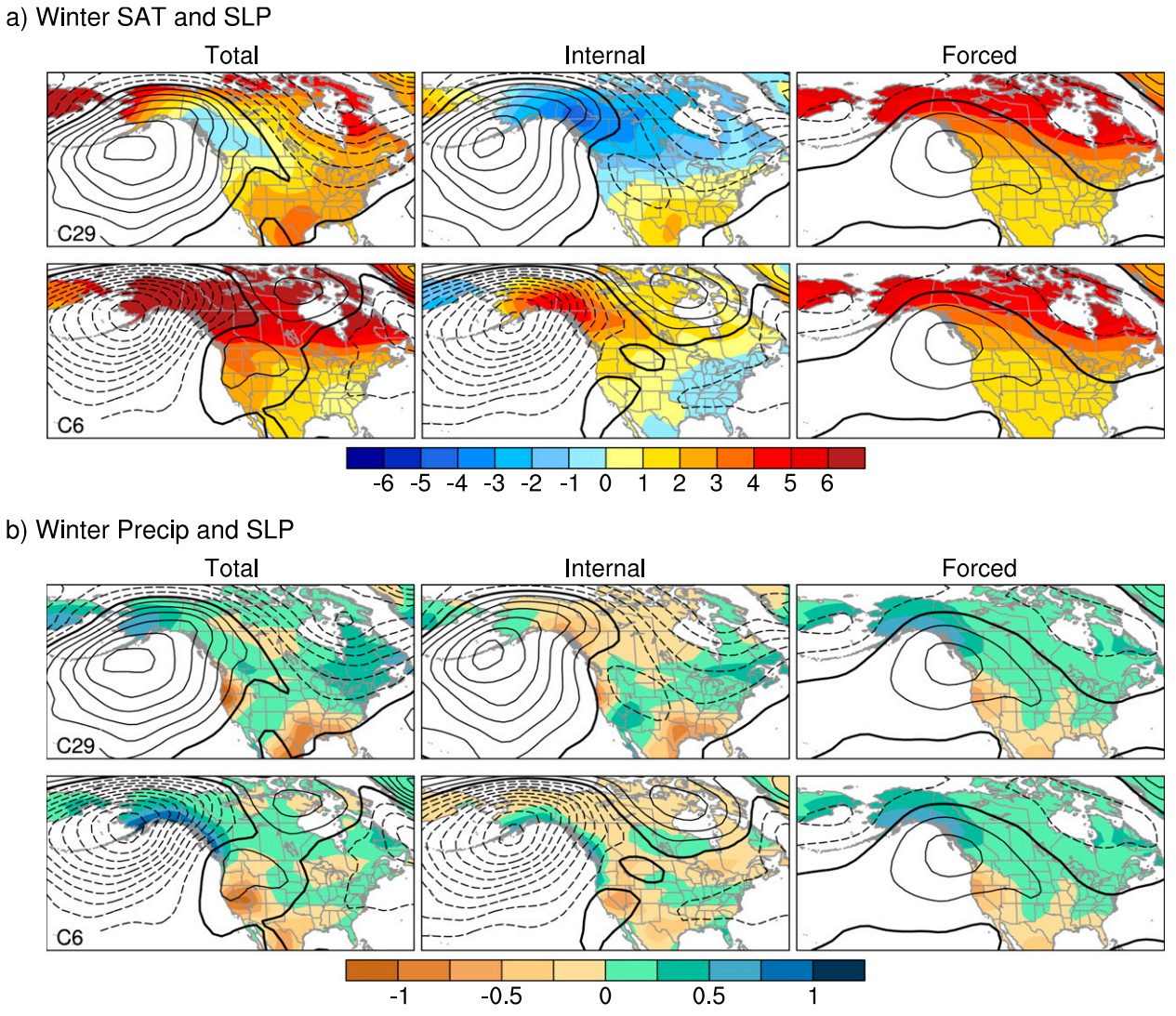

FIG. 10. (left) Total 2010–60 winter trends decomposed into (center) internal and (right) forced components for two contrasting CCSM3 ensemble members (runs 29 and 6) for (a) SAT [color shading; °C $(51\,\mathrm{yr})^{-1}$] and SLP (contours) and (b) precipitation [color shading; mm day^{-1} $(51\,\mathrm{yr})^{-1}$] and SLP (contours). SLP contour interval is 1 hPa $(51\,\mathrm{yr})^{-1}$, with solid (dashed) contours for positive (negative) values; the zero contour is thickened.

that the forced SLP trends are considerably smaller in amplitude than the unforced SLP trends (maximum values ~ 1–2 hPa compared to 6–8 hPa; see also Fig. S7). Indeed, SLP trend signal-to-noise ratios based on the full set of ensemble members are <2 (and mostly <1) over the entire domain in both models and both seasons (Fig. S8).

In addition to SAT, the circulation trends have a clear influence on winter precipitation trends, discernible even in the total fields (Fig. 10b, left). For example, the negative SLP trend in the Gulf of Alaska in run 6 leads to a strong increase in precipitation along the west coast of Canada and southern Alaska compared to run 29, which is under the influence of a blocking high pressure center. In addition, the trough over northeastern Canada in run 29 favors enhanced precipitation compared to run 6, which lacks a pronounced circulation trend in this region. These circulation effects are even more apparent in the unforced component (Fig. 10b, center): the entire west coast from Northern California to eastern Alaska shows reduced (enhanced) precipitation under the influence of the high (low) pressure center to the west in run 29 (6), and much of northeastern Canada shows increased (diminished) precipitation in association with the trough (ridge) to the north in run 29 (6). Unlike SAT, the forced component of the SLP trends has a discernible influence on the forced component of the

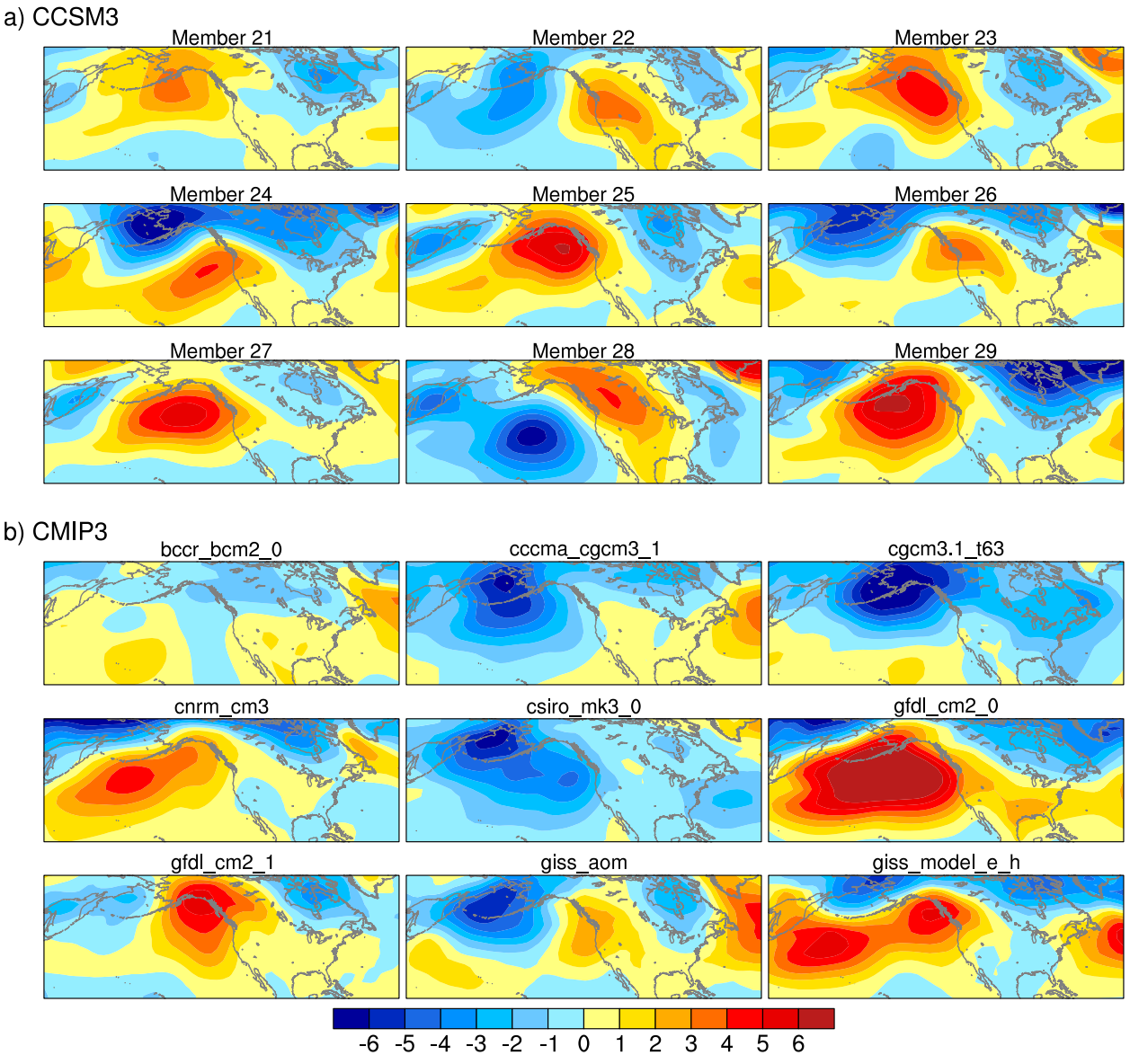

FIG. 11. Winter SLP trends [2010–60; hPa (51 yr)$^{-1}$] from (a) nine individual realizations of CCSM3 (runs 21–29) and (b) nine CMIP3 models, selected alphabetically.

precipitation trends (Fig. 10b, right). In particular, locally enhanced drying (moistening) along the west coast of the United States (Canada) is plausibly a result of the offshore (onshore) flow around the high pressure center. However, the ubiquitous precipitation increase over Canada (~0.2 mm day^{-1}) appears to be thermodynamically induced.

Although the atmospheric circulation is less variable in summer than winter, it also appears to play a role in generating diversity of warm season SAT and precipitation trends within each model ensemble (Figs. S9 and S10). However, as discussed earlier, it may not be possible to confidently separate internal dynamical forcing from thermodynamic land surface feedbacks in some areas such as the central and western United States in summer.

Additional examples of the spread in winter SLP trends within the CCSM3 ensemble are presented in Fig. 11a. These show a wide variety of patterns and polarities among the individual realizations. For example, runs 22, 24, 26, and 28 all show negative SLP trends over the North Pacific and/or Gulf of Alaska, while runs 21, 23, 25, 27, and 29 are dominated by positive trends in these areas. It is clear from this figure that, in any single realization, internal variability makes a larger

contribution than does the GHG-forced response. Similar results obtain for the ECHAM5 ensemble (not shown). For comparison, Fig. 11b shows the winter SLP trends (2010–60) in a single realization from nine different CMIP3 models, chosen alphabetically. The SLP trend patterns and magnitudes within this multimodel ensemble are even more diverse than within the CCSM3 ensemble. For example, the Canadian Centre for Climate Modelling and Analysis (CCCma); Coupled Global Climate Model, version 3.1 (CGCM3); Commonwealth Scientific and Industrial Research Organisation Mark (CSIRO); and Goddard Institute for Space Studies, Atmosphere–Ocean Model (GISS-AOM) models exhibit negative SLP trends over the North Pacific, while the Centre National de Recherches Météorologiques (CNRM); Geophysical Fluid Dynamics Laboratory (GFDL; both versions); and Goddard Institute for Space Studies Model E2, coupled with the Hybrid Coordinate Ocean Model (HYCOM) (GISS-E2H) models have positive trends. The interpretation of the spread in SLP trends within the multimodel ensemble is problematic because of the inclusion of both structural differences among models and internal variability within models. However, visual comparison with the set of CCSM3 runs in Fig. 11a strongly suggests that internal variability may be an important factor, a point also emphasized in Deser et al. (2012b) for the extratropics of both hemispheres. A similar comparison between CCSM3 and CMIP3 for summer SLP trends is shown in Fig. S11.

Empirical orthogonal function (EOF) analysis provides an objective way to identify the most prominent patterns of variability. Here, we have computed the leading EOF of the set of 40 CCSM3 winter SLP trend patterns over the Pacific–North American domain [25°–75°N, 180°–60°W]. Note that, unlike conventional applications of EOF analysis in the time domain, we have applied it in the ''ensemble trend'' domain to find the dominant pattern of internally generated SLP trend variability (see also Deser et al. 2012b). The leading EOF accounts for 59% of the variance in winter SLP trends across the CCSM3 ensemble and is distinct from the second EOF (which accounts for 16% of the variance) according to the criterion of North et al. (1982). This ''dominant'' mode of winter circulation trend variability exhibits, in its positive phase, negative SLP trend anomalies over the North Pacific and weaker downstream centers of alternating sign over the central and southeastern United States (Fig. 12; the downstream features are more apparent at upper levels; not shown). This structure resembles the surface manifestation of the Pacific–North American (PNA) teleconnection pattern (Wallace and Gutzler 1981), a prominent mode of interannual variability in both nature and the model (not shown).

The impact of this circulation pattern upon SAT and precipitation trends is assessed by linearly regressing the set of 40 SAT and precipitation trend values at each grid box upon the standardized SLP principal component (PC) record. Note that the ensemble-mean trends are removed in the linear regression procedure, thereby isolating the internal component of variability. In its positive phase, the SLP trend EOF is accompanied by positive (negative) SAT trend anomalies over the central and western (southeastern) portion of the continent and by positive precipitation trend anomalies along the west coast (Figs. 12a,b). The similarity between these patterns and the unforced trends in ensemble member 6 is noteworthy (recall Figs. 10a,b).

By adding/subtracting this dominant dynamically induced pattern of unforced SAT and precipitation trend variability to/from the forced trends, one obtains the expected range of future changes in SAT and precipitation that results from the superposition of GHG forcing and internal circulation variability (Figs. 12a,b, bottom). Here we have doubled the internal (SLP EOF) contribution to span the 95% range assuming a normally distributed SLP PC. For a -2 standard deviation departure of the SLP PC (σPC), the total (forced plus internal) trends exhibit a strong anticyclonic circulation over the North Pacific (maximum values $\sim$ 9 hPa) and a weaker cyclonic circulation centered over Hudson's Bay, accompanied by relatively modest warming over the northwestern United States (<1°C) and Canada (and slight cooling in Washington and Oregon). This contrasts with the $+2$ σPC case, in which the North Pacific is dominated by negative SLP trends (maximum values $\sim$ -8 hPa), accompanied by considerably larger warming (3°–4°C) over the Pacific northwest and muted warming (<1°C) over the southeast (Fig. 12a, bottom right). Similarly, the -2 σPC case shows a north–south dipole pattern of precipitation trends along the west coast of North America with a nodal line over British Columbia, compared to the $+2$ σPC case in which the nodal line is shifted southward over Northern California (Fig. 12b, bottom). The correspondence between these ''endmember'' precipitation trend patterns and the raw trends in ensemble members 6 and 29 (recall Figs. 10a,b) is noteworthy.

This example serves to illustrate the effects of unforced circulation-induced trends in the presence of GHG-forced climate change. Of course, other circulation trend patterns will complicate the picture in any given model run but, to the extent that this is the dominant mode of circulation trend variability, it provides some guidance on the range of unforced circulation-induced SAT and precipitation trends that will be superimposed upon the GHG-forced response. Analogous results are found for summer, although the leading EOF of SLP trends accounts for a smaller proportion of variance (40%) than in winter (Fig. S12).

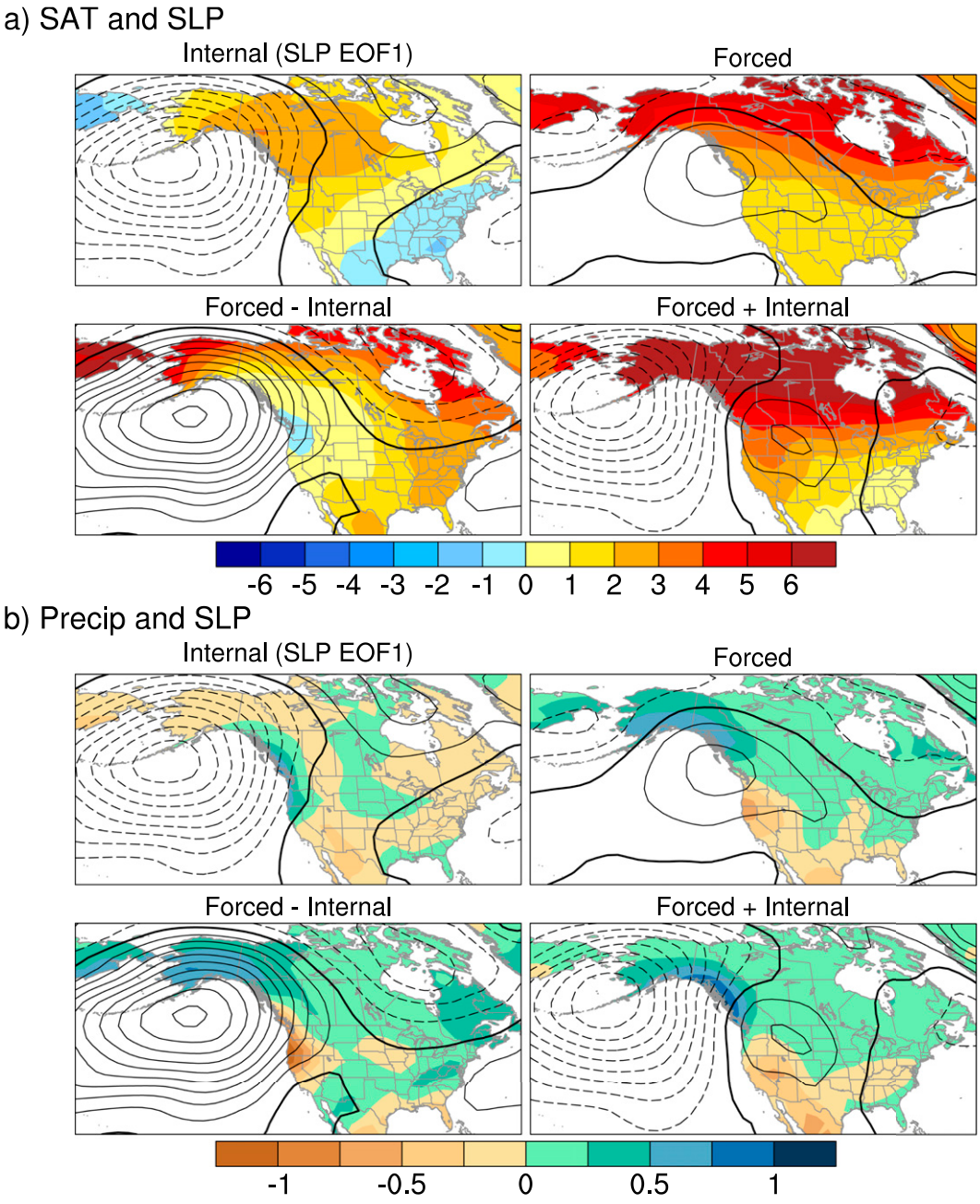

FIG. 12. a) (top left) Regressions of winter SLP and SAT trends upon the leading PC of winter SLP trends in the 40-member CCSM3 ensemble, where values have been multiplied by 2; (top right) CCSM3 ensemble-mean winter SLP and SAT trends; (bottom left) difference of (top right) minus (top left); and (bottom right) sum of (top right) plus (top left). (b) As in (a), but substituting precipitation for SAT. Contour interval is 1 hPa $(51\ \text{yr})^{-1}$; color shading in units of degrees Celsius per 51 yr for SAT and millimeters per day per 51 yr for precipitation.

f. Dynamical adjustment of the SAT and precipitation trends

It is clear from the results shown above that the large-scale atmospheric circulation affects the spatial patterns and magnitudes of regional SAT and precipitation trends in any given model realization by virtue of its large natural variability, obfuscating the anthropogenically forced signal. To further demonstrate the confounding impact of dynamically induced internal variability upon climate trends in any single GHG-forced simulation, we have constructed "dynamically

TABLE 1. Cumulative percentages of winter (DJF) and summer (JJA) SAT and precipitation (PPT) 2010–60 trend variance explained by the first, second, and third SLP predictor patterns, averaged over all North American grid boxes in the top half of the table. The bottom half of the table is as in the top but for the signal-to-noise ratios of the dynamically adjusted trends. C40 refers to the 40-member CCSM3 ensemble, and E17 refers to the 17-member ECHAM5 ensemble. See text for details.

	Cumulative percentage of trend variance (%)							
SLP predictor pattern	C40 SAT DJF	C40 SAT JJA	C40 PPT DJF	C40 PPT JJA	E17 SAT DJF	E17 SAT JJA	E17 PPT DJF	E17 PPT JJA
1	55	54	45	35	54	55	46	50
2	70	67	66	52	80	77	75	73
3	80	78	75	65	90	90	88	87
	Signal-to-noise ratios of the dynamically adjusted trends							
SLP predictor pattern	C40 SAT DJF	C40 SAT JJA	C40 PPT DJF	C40 PPT JJA	E17 SAT DJF	E17 SAT JJA	E17 PPT DJF	E17 PPT JJA
1	3.8	4.6	1.2	0.8	5.2	6.3	1.2	0.8
2	4.7	5.4	1.4	0.9	7.8	8.9	1.7	1.1
3	5.6	6.7	1.7	1.1	11.7	13.8	2.4	1.6
Unadjusted	2.6	3.1	0.9	0.6	3.4	4.2	0.9	0.5

adjusted'' versions of the SAT and precipitation trends for each member of the CCSM3 and ECHAM5 ensembles following the method of Wallace et al. (2012) and Smoliak (2013). Briefly, three orthogonal SLP trend predictor patterns are determined for SAT (or precipitation) trends at each grid box using the method of partial least squares. Our choice of three SLP predictors is motivated by the fact that the additional trend variance explained by the fourth predictor is small (<5%) and because the first three predictor patterns are all clearly physically meaningful (not shown). However, the results are not sensitive to the exact number of SLP predictor patterns or to the precise domain used for calculating them (here we use the same domain as in the SLP EOF analysis above). Other methods of dynamical adjustment—for example, using SLP trend EOFs as predictor patterns—yield similar results (not shown).

Table 1a shows the cumulative percentages of SAT and precipitation trend variance explained by the first, second and third SLP predictor patterns, averaged over all North American grid boxes. These predictors achieve cumulative reductions in trend variance of 35%–55%, 52%–70%, and 65%–80%, respectively, for CCSM3 (46%–55%, 73%–80%, and 87%–90%, respectively, for ECHAM5), with the ranges denoting the dependence on season and reference variable. The remaining fraction of unexplained trend variance is attributable to thermodynamic processes and to unresolved dynamical influences.

Figures 13 and 14 compare the total and dynamically adjusted SAT and precipitation trends for the contrasting CCSM3 ensemble members discussed earlier for winter (Fig. 10) and summer (Fig. S8). It is clear that by reducing the circulation-induced component of internal trend variability, the individual runs are brought into much better agreement, consistent with the results in Table 1a. Additionally, the dynamically adjusted trend patterns resemble more closely the forced component of the response than the raw trends, as expected. These examples serve as powerful demonstrations of the impact of internally generated circulation trends upon SAT and precipitation trends in any single GHG-forced model simulation.

As alluded to earlier, comparing projected climate trends from single realizations of different models is problematic because of the confounding effects of structural differences between models (which can lead to different forced responses) and the presence of internal variability. Figures 15 and 16 illustrate how the reduction of internally generated dynamical contributions to single contrasting runs from the CCSM3 and ECHAM5 models clarifies their comparison. The SAT and precipitation trends in the two models show much better agreement after accounting for the effects of internally generated circulation trends. Remaining differences can be largely attributed to differences in their forced responses (Figs. 15 and 16, right).

Reducing the influence of internal circulation trends from the SAT and precipitation trends also augments their SNR (Table 1b). The average SNR over North America increases by approximately a factor of 2–3 after dynamical adjustment with three orthogonal SLP predictor patterns. In particular, SAT SNR increases from ~3 to ~6 in CCSM3 and from ~4 to ~12 in ECHAM5 in both seasons. Although the fractional increase in SNR for precipitation is similar to that for

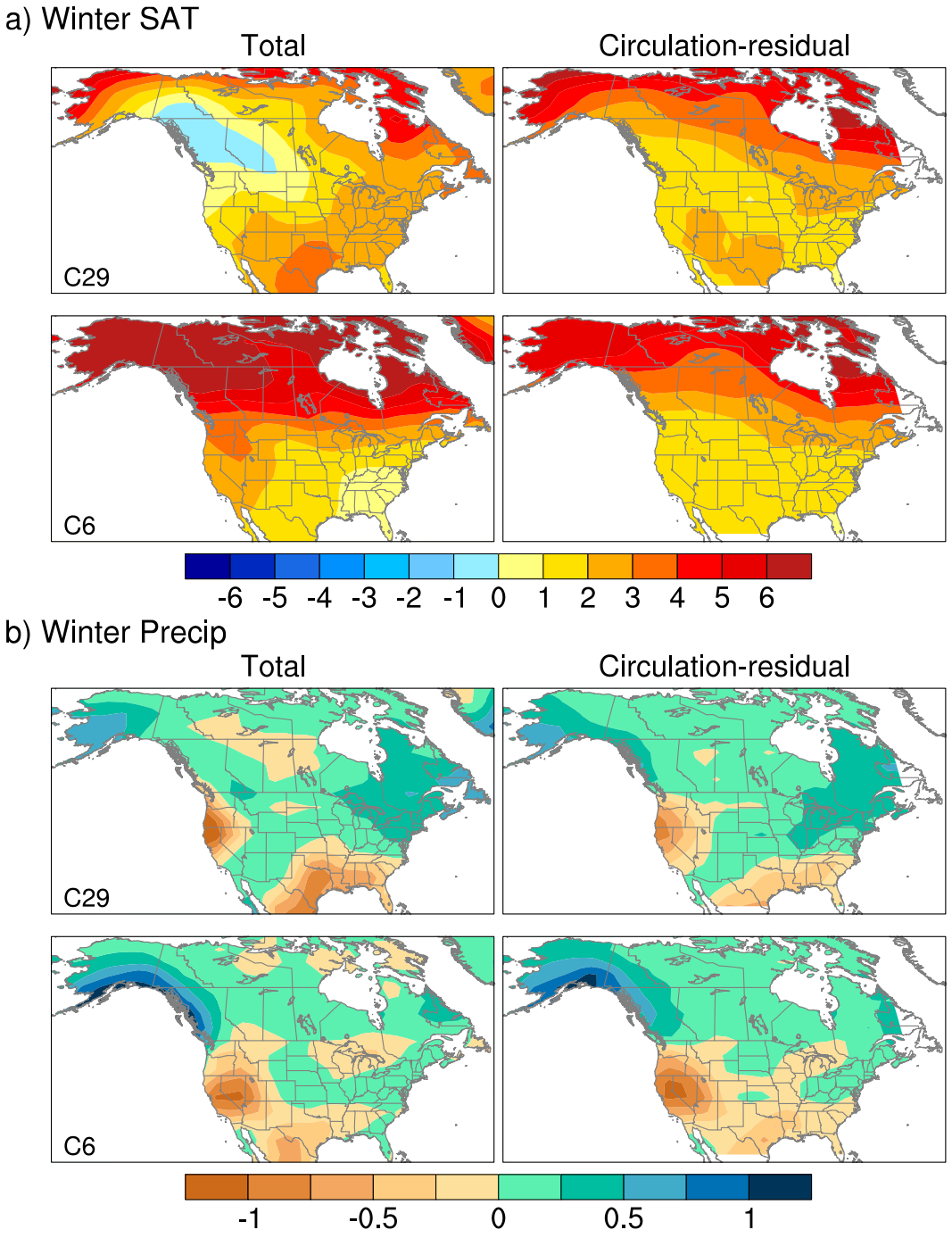

FIG. 13. Winter (a) SAT [°C (51 yr)$^{-1}$] and (b) precipitation [mm day^{-1} (51 yr)$^{-1}$] trends (2010–60) for two contrasting CCSM3 ensemble members (runs 29 and 6) based on (left) total and (right) dynamically adjusted ("circulation residual") fields. See text for details.

SAT, it remains relatively low even with three SLP predictors (~2 in winter and ~1 in summer). This may reflect a combination of factors, including a weak forced signal (Fig. 7a), thermodynamically generated internal variability, and dynamically induced internal variability unresolved by three large-scale predictor patterns. We note that the average precipitation SNR after dynamical adjustment is higher for Canada and Alaska (1.6 in CCSM3 and 2.7 in ECHAM5) than for the contiguous United States (0.8 in CCSM3 and 1.9 in ECHAM5),

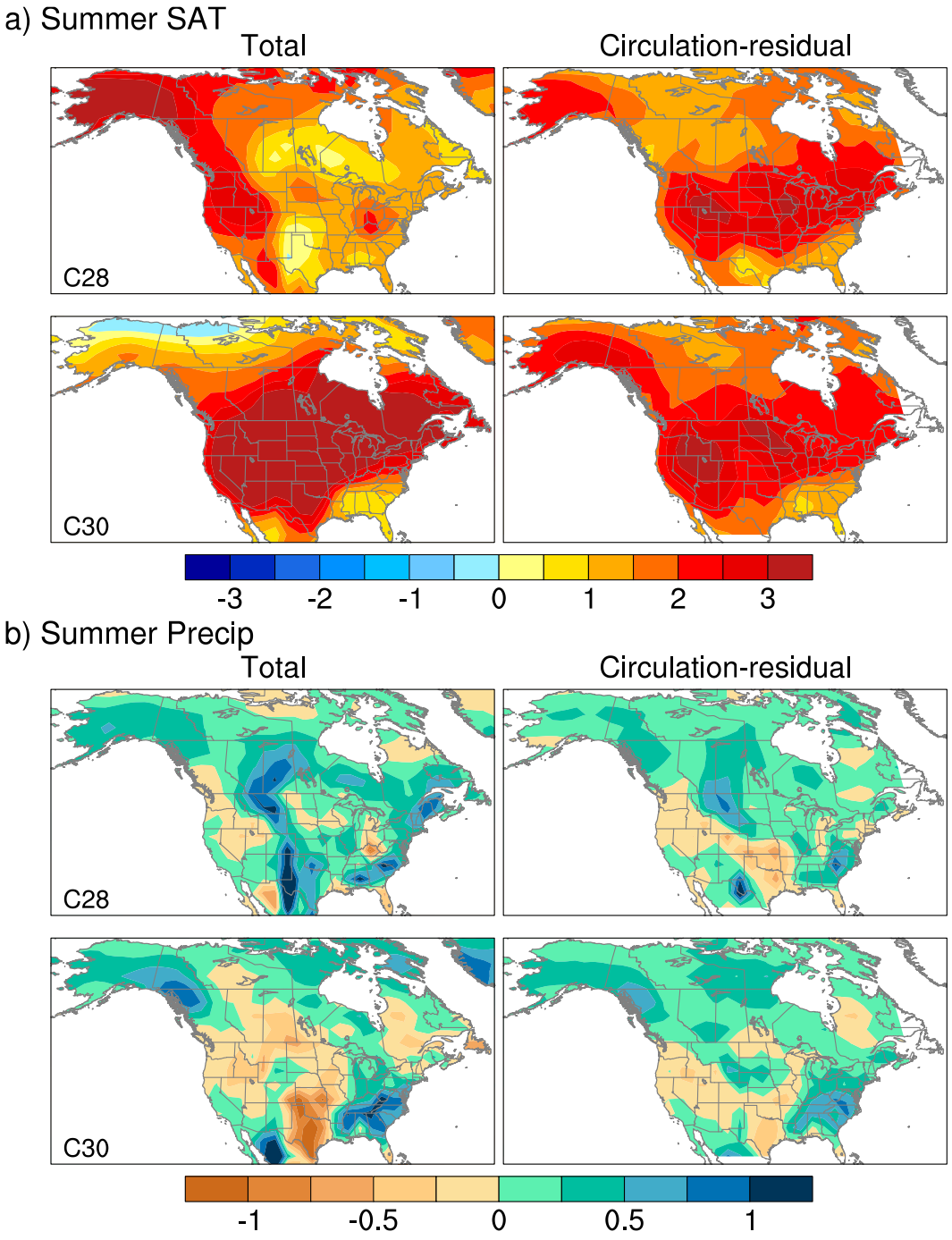

FIG. 14. As in Fig. 13, but for summer: CCSM3 runs 28 and 30.

consistent with the stronger forced component of the response at high latitudes (recall Fig. 7a).

g. Assessing the models' multidecadal variability

An important consideration in assessing the relevance of the results from the multimember CCSM3 and ECHAM5 ensembles for the real world is the fidelity with which the models simulate the variability of 50-yr climate trends. While the limited duration of the observational record precludes a direct assessment of 50-yr trend variance, the magnitudes of observed and simulated variability on decadal-to-multidecadal time scales can be compared. Figure 17 shows maps of the standard deviation of 8-yr low-pass filtered SAT, precipitation,

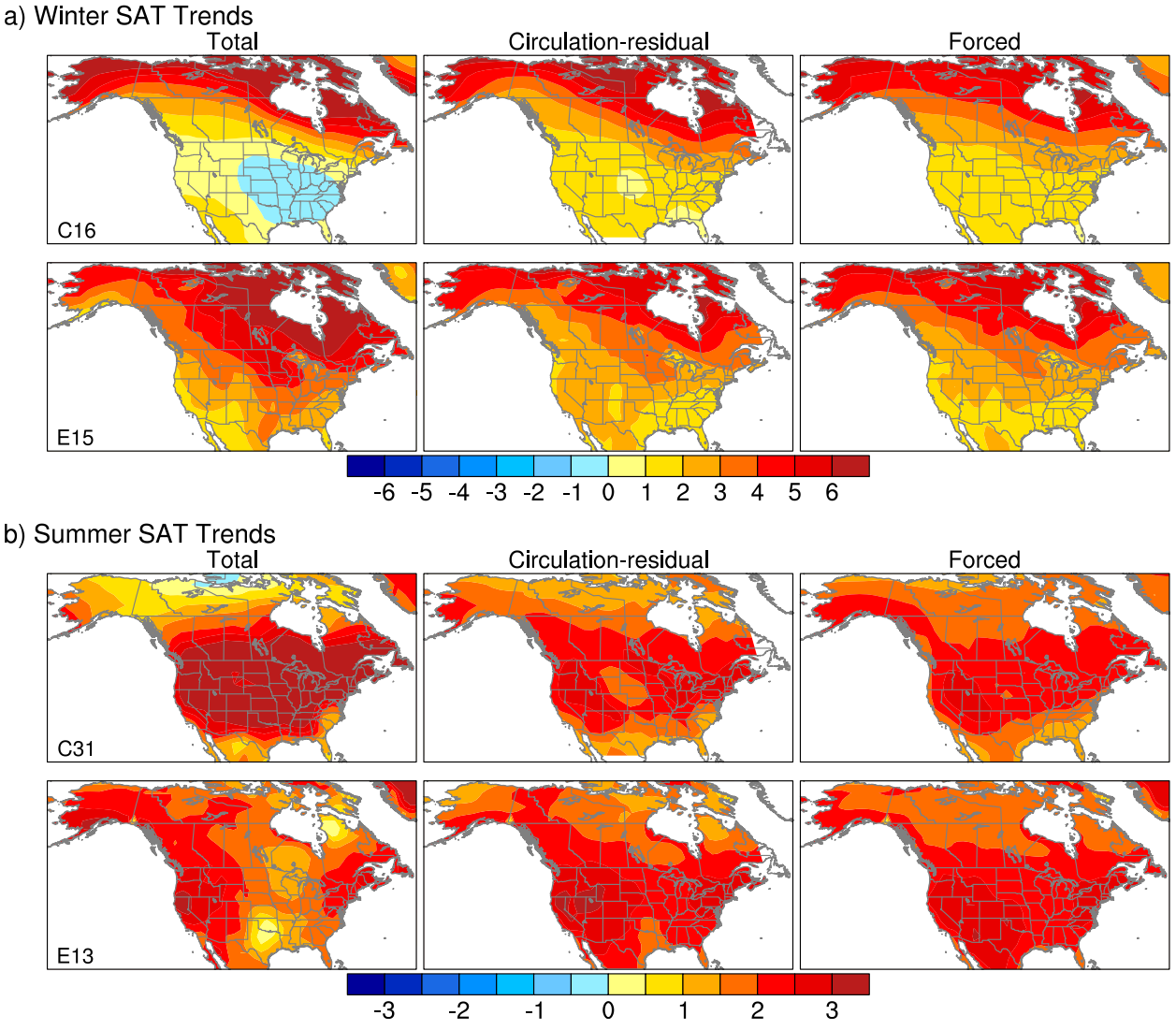

FIG. 15. SAT trends (2010–60) in (a) winter and (b) summer for a single realization of (top) CCSM3 and (bottom) ECHAM5 based on (left) total and (center) dynamically adjusted (circulation residual) fields. (right) The ensemble-mean (e.g., forced) trends in (top) CCSM3 and (bottom) ECHAM5. Color bar is in units of degrees Celsius per 51 yr.

and SLP anomalies in winter and summer from the models and ~110 yr of observations (see datasets listed in section 2; similar results are obtained with other datasets: not shown). To reduce the influence of potential externally forced signals, we have removed the linear trend from the observations, although this has almost no effect (not shown). For the same reason, we also removed the ensemble mean from each model run at each time step. The low-pass filtered time series from each model run were appended to one another before computing the standard deviation of this overall record.

The magnitudes and spatial patterns of decadal SAT and precipitation variability are reasonably well simulated by both models (Figs. 17a,b, respectively). Observed SAT in winter shows a band of high decadal variance extending from Alaska southeastward across the continent: this structure is relatively well captured by ECHAM5 and less well simulated by the coarser-resolution CCSM3 but overall magnitudes are similar. Observed SAT in summer shows a more homogenous pattern of decadal variance compared to winter, an aspect that is well simulated by the models; the magnitudes are well represented by ECHAM5 and overestimated by ~20%–30% in CCSM3. The observed winter precipitation variance maxima along the west coast of North America and the southeastern United States are reproduced in the models, with the magnitudes somewhat underestimated in CCSM3. Observed summer precipitation variance is more evenly

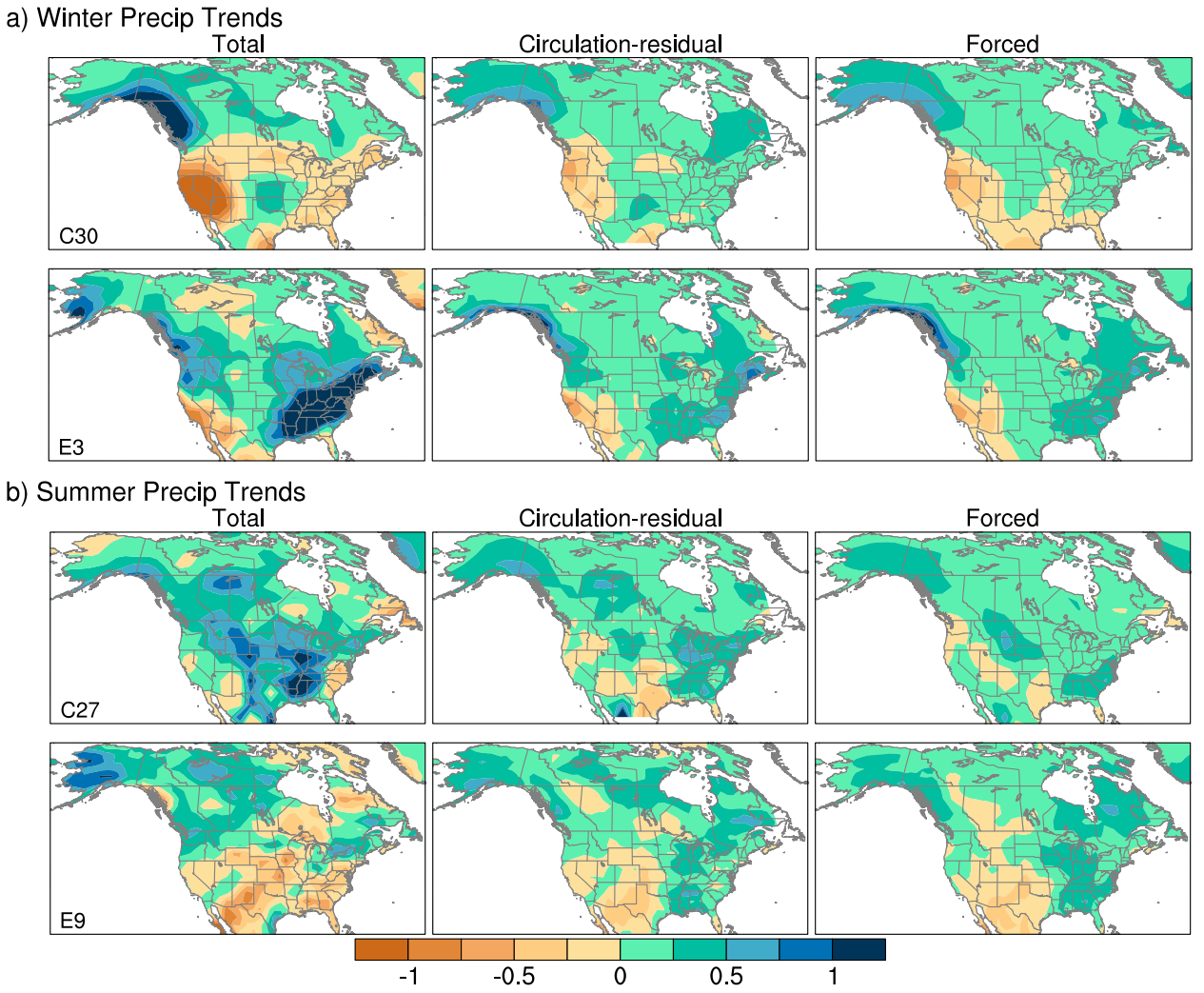

FIG. 16. As in Fig. 15, but for precipitation [mm day^{-1} (51 yr)$^{-1}$].

distributed across the continent than in winter, increasing gradually from west to east across the United States. This aspect is generally captured by the models, in terms of both pattern and overall magnitude.

Observed winter SLP shows a center of enhanced decadal variance over the North Pacific (maximum values ~ 3 hPa) as well as higher variance over Canada (~1–2 hPa) compared to the United States (~0.5–1 hPa; Fig. 17c). The models simulate these features, although CCSM3 overestimates the variance over the North Pacific and northwestern North America by ~20%–30%. The observed reduction in SLP variance in summer compared to winter is captured by the models, with a slight underestimate of the simulated summer SLP variance over the United States.

In summary, the comparisons shown in Fig. 17 indicate that the models simulate generally realistic distributions of low-frequency (>8 yr) variability in SAT, precipitation, and SLP, with magnitudes mostly within 20%–30% of observations. Additional information on the temporal characteristics and spatial patterns of simulated multidecadal climate variability may be found in special issue on CCSM3 of the *Journal of Climate* (2006, Vol. 19, No. 11) and the special issue section on ECHAM5 of the *Journal of Climate* (2003, Vol. 19, No. 16). Further work is needed to assess the fidelity of simulated multidecadal variability, including the models' representations of mechanisms and feedbacks.

4. Summary and discussion

We have examined the contribution of internal variability to uncertainty in projected SAT and precipitation trends during the next 50 yr at local and regional scales

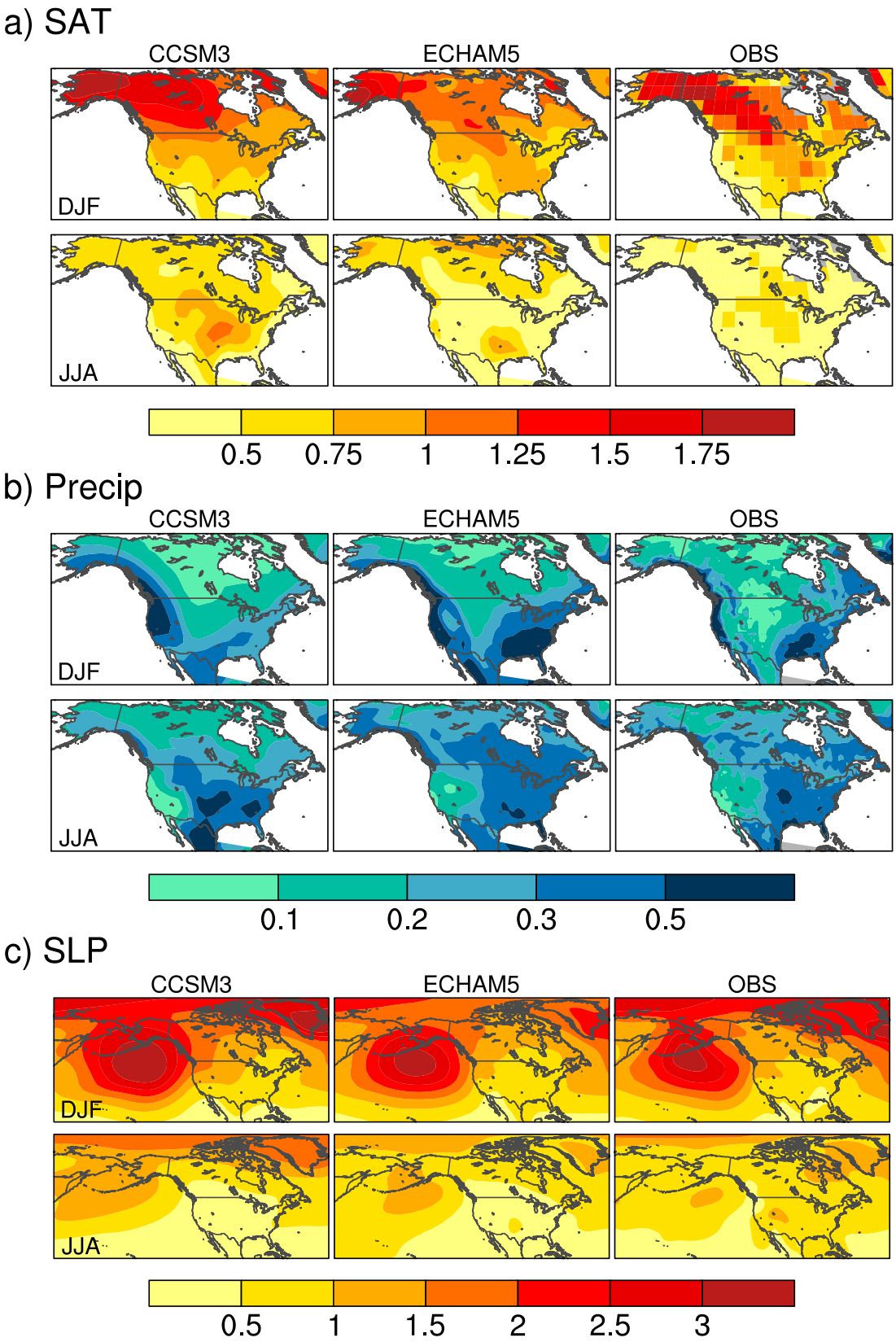

FIG. 17. Amplitude of decadal variability in CCSM3, ECHAM5, and observations for (a) SAT (°C), (b) precipitation (mm day^{-1}), and (c) SLP (hPa) in (top) winter and (bottom) summer.

over North America from large ensembles of simulations with two comprehensive climate models. Each simulation is subject to the identical GHG forcing scenario (SRES A1B) but begins from a different atmospheric initial condition: thus, the spread of future climate trends is attributable to unpredictable internally generated variability. Unlike multimodel ensembles such as CMIP3 and CMIP5, which confound internal variability and structural differences among models, our experimental design allows us to isolate the contribution of internal variability to the spread of anthropogenically forced climate projections. Consistent results are found for both model ensembles, including higher relative uncertainty in projected trends for precipitation compared to SAT regardless of season and for SAT in winter compared to summer. This uncertainty stems in large part from the dynamical effects of atmospheric circulation trends that contain a high proportion of unforced variability compared to GHG-forced signals. The broad spatial scale of these circulation changes imparts regional coherence to the internal component of surface climate trends in any single model run. This in turn has important consequences for impacts upon agricultural and water resources, as wide areas within the United States and Canada are affected in a similar manner.

By elucidating the impact of natural circulation-induced climate trends, we provide a new perspective on how to usefully compare climate change projections across models and how to properly interpret the single climate trajectory that nature will produce. This new perspective highlights the importance of conducting numerous simulations with a given climate model, as each realization will contain a different mix of unforced and forced changes. Indeed, we advocate that, for the next International Panel on Climate Change (IPCC) assessment, modeling centers consider allocating resources in favor of large ensembles, even at the cost of prescribing alternate forcing scenarios. The minimum number of ensemble members needed will depend on the climate parameter, geographical location, spatial scale, and time horizon of interest (see Deser et al. 2012b; Screen et al. 2013). Lengthy model control integrations provide an additional resource for obtaining relevant information on internal variability, and when combined with estimates of the forced response can be used to enhance ensembles of climate change simulations. Alternatively, statistics of unforced variability derived from observations can be used in place of model estimates of internal variability.

In analogy with ensemble weather forecasting, this study underscores the need for ensemble climate forecasts to inform public policy, planning, and mitigation efforts. Even over time spans as long as the next 50 yr, natural climate variability superimposed upon forced climate change will result in range of possible future climate trends. As in seasonal forecasting, this range can be represented as a distribution from which the likelihood of a particular trend outcome or threshold exceedance can be determined. Such distributions can be used to assess vulnerability and risk for a broad range of climate impacts: for example, wildfires and human health hazards, including effects on extreme events such as heat waves, floods, and droughts. We reiterate that any single model run or any multimodel average (e.g., from CMIP3/5) lacks information on the expected range of climate trend outcomes associated with natural variability, limiting utility for decision-making purposes. By the same token, regional climate models and statistical/dynamical downscaling procedures should make use of the range of ensemble climate forecasts conducted with global models. These efforts should also incorporate information on the reliability of ensemble climate forecasts as discussed in van Oldenborgh et al. (2013).

Our study has focused on North America. Preliminary results indicate that similar uncertainties in future climate trends are present over Eurasia (not shown). Other regions of the globe, however, may contain a higher proportion of human-induced climate change compared to natural variability than the northern continents: in particular, low-latitude areas whose populations are particularly vulnerable to climate fluctuations (Mahlstein et al. 2011; Wallace et al. 2014). Further work on the relative roles and mechanisms of internally generated and forced climate change in other regions is warranted.

Acknowledgments. We thank Dr. Haiyan Teng for assistance with the CCSM3 ensemble and Dr. Grant Branstator and Professor John M. Wallace for useful discussions during the course of this work. We also thank the three anonymous reviewers for their comments and suggestions.

REFERENCES

Becher, A., P. Finger, A. Meyer-Christoffer, B. Rudolf, K. Schamm, U. Schneider, and M. Ziese, 2013: A description of the global land-surface precipitation data products of the Global Precipitation Climatology Centre with sampling applications including centennial trend analysis from 1901–present. *Earth Syst. Sci. Data,* **5,** 71–99.

Branstator, G. W., H. Teng, G. A. Meehl, M. Kimoto, J. R. Knight, M. Latif, and A. Rosati, 2012: Systematic estimates of initial-value decadal predictability for six AOGCMs. *J. Climate,* **25,** 1827–1846.

Compo, G. P., and Coauthors, 2011: The Twentieth Century Reanalysis Project. *Quart J. Roy. Meteor. Soc.,* **137,** 1–28.

Deser, C., A. S. Phillips, and J. W. Hurrell, 2004: Pacific interdecadal climate variability: Linkages between the tropics and

North Pacific during boreal winter since 1900. *J. Climate,* **17,** 3109–3124.

——, R. Knutti, S. Solomon, and A. S. Phillips, 2012a: Communication of the role of natural variability in future North American climate. *Nat. Climate Change,* **2,** 775–779, doi:10.1038/nclimate1562.

——, A. S. Phillips, V. Bourdette, and H. Teng, 2012b: Uncertainty in climate change projections: The role of internal variability. *Climate Dyn.,* **38,** 527–546, doi:10.1007/s00382-010-0977-x.

Enfield, D. B., A. M. Mestas-Nunez, and P. J. Trimble, 2001: The Atlantic multidecadal oscillation and its relation to rainfall and river flows in the continental U.S. *Geophys. Res. Lett.,* **28,** 2077–2080.

Feldstein, S. B., 2000: The timescale, power spectra, and climate noise properties of teleconnection patterns. *J. Climate,* **13,** 4430–4440.

Fischer, E. M., S. I. Seneviratne, D. Lüthi, and C. Schär, 2007: Contribution of land-atmosphere coupling to recent European summer heat waves. *Geophys. Res. Lett.,* **34,** L06707, doi:10.1029/2006GL029068.

Hawkins, E., and R. Sutton, 2009: The potential to narrow uncertainty in regional climate predictions. *Bull. Amer. Meteor. Soc.,* **90,** 1095–1107.

——, and ——, 2011: The potential to narrow uncertainty in projections of regional precipitation change. *Climate Dyn.,* **37,** 407–418, doi:10.1007/s00382-010-0810-6.

Hoerling, M., J. Eischeid, A. Kumar, R. Leung, A. Mariotti, K. Mo, S. Schubert, and R. Seager, 2014: Causes and predictability of the 2012 Great Plains drought. *Bull. Amer. Meteor. Soc.,* in press.

Horel, J. D., and J. M. Wallace, 1981: Planetary-scale atmospheric phenomena associated with the Southern Oscillation. *Mon. Wea. Rev.,* **109,** 813–829.

Hu, A., and C. Deser, 2013: Uncertainty in future regional sea level rise due to internal climate variability. *Geophys. Res. Lett.,* **40,** 2768–2772, doi:10.1002/grl.50531.

Hurrell, J. W., 1996: Influence of variations in extratropical wintertime teleconnections on Northern Hemisphere temperatures. *Geophys. Res. Lett.,* **23,** 665–668.

Kang, S. M., C. Deser, and L. M. Polvani, 2013: Uncertainty in climate change projections of the Hadley circulation: The role of internal variability. *J. Climate,* **26,** 7541–7554.

Lorenz, E. N., 1963: Deterministic nonperiodic flow. *J. Atmos. Sci.,* **20,** 130–141.

Mahlstein, I., R. Knutti, S. Solomon, and R. W. Portmann, 2011: Early onset of significant local warming in low latitude countries. *Environ. Res. Lett.,* **6,** 034009, doi:10.1088/1748-9326/6/3/034009.

Mantua, N. J., S. R. Hare, Y. Zhang, J. M. Wallace, and R. Francis, 1997: A Pacific interdecadal climate oscillation with impacts on salmon production. *Bull. Amer. Meteor. Soc.,* **78,** 1069–1079.

Matei, D., H. Pohlmann, J. Jungclaus, W. Müller, H. Haak, and J. Marotzke, 2012: Two tales of initializing decadal climate prediction experiments with the ECHAM5/MPI-OM model. *J. Climate,* **25,** 8502–8523.

Meehl, G. A., and Coauthors, 2006: Climate change projections for the twenty-first century and climate change commitment in the CCSM3. *J. Climate,* **19,** 2597–2616.

——, J. M. Arblaster, and G. Branstator, 2012: Mechanisms contributing to the warming hole and the consequent U.S. east–west differential of heat extremes. *J. Climate,* **25,** 6394–6408.

——, A. Hu, J. Arblaster, J. Fasullo, and K. Trenberth, 2013: Externally forced and internally generated decadal climate variability associated with the interdecadal Pacific oscillation. *J. Climate,* **26,** 7298–7310.

Minobe, S., 1997: A 50–70 year climatic oscillation over the North Pacific and North America. *Geophys. Res. Lett.,* **24,** 683–686.

Msadek, R., K. W. Dixon, T. L. Delworth, and W. Hurling, 2010: Assessing the predictability of the AMOC and associated fingerprints. *Geophys. Res. Lett.,* **37,** L19608, doi:10.1029/2010GL044517.

Newman, M., 2007: Interannual to decadal predictability of tropical and North Pacific sea surface temperatures. *J. Climate,* **20,** 2333–2356.

——, 2013: An empirical benchmark for decadal forecasts of global surface temperature anomalies. *J. Climate,* **26,** 5260–5269.

North, G. R., F. J. Moeng, T. J. Bell, and R. F. Cahalan, 1982: Sampling errors in the estimation of empirical orthogonal functions. *Mon. Wea. Rev.,* **110,** 699–706.

Oshima, K., Y. Tanimoto, and S.-P. Xie, 2012: Regional patterns of wintertime SLP change over the North Pacific and their uncertainty in CMIP3 multi-model projections. *J. Meteor. Soc. Japan,* **90,** 385–396, doi:10.2151/jmsj.2012-A23.

Power, S. B., T. Casey, C. Folland, A. Colman, and V. Mehta, 1999: Interdecadal modulation of the impact of ENSO on Australia. *Climate Dyn.,* **15,** 319–324.

Roeckner, E., and Coauthors, 2003: The atmospheric general circulation model ECHAM5. Part I: Model description. Max-Planck-Institut für Meteorologie Rep. 349, 140 pp.

Santer, B. D., and Coauthors, 2011: Separating signal and noise in atmospheric temperature changes: The importance of timescale. *J. Geophys. Res.*, **116,** D22105, doi:10.1029/2011JD016263.

Screen, J. A., C. Deser, I. Simmonds, and R. Tomas, 2013: Atmospheric impacts of Arctic sea-ice loss, 1979–2009: Separating forced change from atmospheric internal variability. *Climate Dyn.,* doi:10.1007/s00382-013-1830-9.

Smoliak, B. V., 2013: Detection and attribution of surface air temperature change in the instrumental record. Ph.D. thesis, University of Washington, 190 pp.

Solomon, S., D. Qin, M. Manning, Z. Chen, M. Marquis, K. Averyt, M. Tignor, and H. L. Miller Jr., Eds., 2007: *Climate Change 2007: The Physical Science Basis.* Cambridge University Press, 996 pp.

Sterl, A., and Coauthors, 2008: When can we expect extremely high surface temperatures? *Geophys. Res. Lett.,* **35,** L14703, doi:10.1029/2008GL034071.

Thompson, D. W. J., J. M. Wallace, P. D. Jones, and J. J. Kennedy, 2009: Identifying signatures of natural climate variability in time series of global mean surface temperature: Methodology and insights. *J. Climate,* **22,** 6120–6141.

Ting, M., Y. Kushnir, R. Seager, and C. H. Li, 2009: Forced and internal twentieth-century SST trends in the North Atlantic. *J. Climate,* **22,** 1469–1481.

——, ——, ——, and L. Cuihua, 2011: Robust features of Atlantic multi-decadal variability and its climate impacts. *Geophys. Res. Lett.,* **38,** L17705, doi:10.1029/2011GL048712.

Trenberth, K. E., and D. J. Shea, 2005: Relationships between precipitation and surface temperature. *Geophys. Res. Lett.,* **32,** L14703, doi:10.1029/2005GL022760.

van Oldenborgh, G. J., F. J. Doblas Reyes, S. S. Drijfhout, and E. Hawkins, 2013: Reliability of regional climate model trends. *Environ. Res. Lett.,* **8,** 014055, doi:10.1088/1748-9326/8/1/014055.

Vose, R. S., and Coauthors, 2012: NOAA's Merged Land–Ocean Surface Temperature analysis. *Bull. Amer. Meteor. Soc.,* **93,** 1677–1685.

Wallace, J. M., and D. S. Gutzler, 1981: Teleconnections in the geopotential height field during the Northern Hemisphere winter. *Mon. Wea. Rev.,* **109,** 784–812.

——, Y. Zhang, and J. A. Renwick, 1995: Dynamic contribution to hemispheric mean temperature trends. *Science,* **270,** 780–783.

——, Q. Fu, B. V. Smoliak, P. Lin, and C. M. Johanson, 2012: Simulated versus observed patterns of warming over the extratropical Northern Hemisphere continents during the cold season. *Proc. Natl. Acad. Sci. USA,* **109,** 14 332–14 337.

——, C. Deser, B. V. Smoliak, and A. S. Phillips, 2014: Attribution of climate change in the presence of internal variability. *Climate Change: Multidecadal and Beyond,* C. P. Chang et al., Eds., Asia-Pacific Weather and Climate Series, Vol. 6, World Scientific, in press.

Wettstein, J. J., and C. Deser, 2014: Internal variability in projections of twenty-first century Arctic sea ice loss: Role of the large-scale atmospheric circulation. *J. Climate,* **27,** 527–550.

Wunsch, C., 1999: The interpretation of short climate records, with comments on the North Atlantic and Southern Oscillations. *Bull. Amer. Meteor. Soc.,* **80,** 245–255.

Zhang, R., and T. Delworth, 2006: Impact of Atlantic multidecadal oscillations on India/Sahel rainfall and Atlantic hurricanes. *Geophys. Res. Lett.,* **33,** L17712, doi:10.1029/2006GL026267.